MNRAS 000, 1–19 (2011) Preprint 28 July 2015 Compiled using MNRAS LATEX style file v3.0

The evolving relation between star-formation rate and stellar mass in the VIDEO Survey since $z = 3$

Russell Johnston,[1,5⋆] Mattia Vaccari,[1,6] Matt Jarvis,[2,1] Mathew Smith,[1,4] Elodie Giovannoli,[1] Boris Häußler[2,3] and Matthew Prescott[1]

[1]*Physics Department, University of the Western Cape, Cape Town 7535, South Africa*
[2]*Astrophysics, University of Oxford, Keble Road, Oxford, OX1 3RH, UK*
[3]*Centre for Astrophysics, Science & Technology Research Institute, University of Hertfordshire, Hatfield, Herts AL10 9AB, UK*
[4]*School of Physics and Astronomy, University of Southampton, Southampton SO17 1BJ*
[5]*South African Astronomical Observatory, P.O. Box 9, Observatory 7935, South Africa*
[6]*INAF - Istituto di Radioastronomia, via Gobetti 101, 40129 Bologna, Italy*

Accepted XXX. Received YYY; in original form ZZZ

ABSTRACT

We investigate the star-formation rate (SFR) and stellar mass, M_* relation of a star-forming (SF) galaxy sample in the XMM-LSS field to $z \sim 3.0$ using the near-infrared data from the VISTA Deep Extragalactic Observations (VIDEO) survey. Combining VIDEO with broad-band photometry, we use the SED fitting algorithm CIGALE to derive SFRs and M_* and have adapted it to account for the full photometric redshift PDF uncertainty. Applying a SF selection using the D4000 index, we find evidence for strong evolution in the normalisation of the SFR-M_* relation out to $z \sim 3$ and a roughly constant slope of (SFR $\propto M_*^{\alpha}$) $\alpha = 0.69 \pm 0.02$ to $z \sim 1.7$. We find this increases close to unity toward $z \sim 2.65$. Alternatively, if we apply a colour selection, we find a distinct turnover in the SFR-M_* relation between $0.7 \lesssim z \lesssim 2.0$ at the high mass end, and suggest that this is due to an increased contamination from passive galaxies. We find evolution of the specific SFR $\propto (1+z)^{2.60}$ at $\log_{10}(M_*/M_{\odot}) \sim 10.5$, out to $z \lesssim 2.4$ with an observed flattening beyond $z \sim 2$ with increased stellar mass. Comparing to a range of simulations we find the analytical scaling relation approaches, that invoke an equilibrium model, a good fit to our data, suggesting that a continual smooth accretion regulated by continual outflows may be a key driver in the overall growth of SFGs.

Key words: galaxies: evolution-galaxies: stellar content-infrared: galaxies : methods: statistical: infrared: galaxies

1 INTRODUCTION

Quantifying the interplay between star formation and stellar mass (M_*) is a crucial component to understanding the build up of galaxies over cosmic time. Whilst early works established the decline in SFR as a function of redshift (e.g. Madau 1995; Lilly et al. 1996; Hopkins & Beacom 2006), the recent acquisition of data from broad band photometry coupled with access to deep and wide galaxy surveys, led to Noeske et al. (2007a) demonstrating a strong correlation between star-formation rate (SFR) and M_* out to $z \sim 1$, which they termed the star forming 'Main Sequence' (SF-MS). This SF-MS was modelled by a simple power-law of the form SFR=βM_*^{α} where strong evolution in the normalisation results in a rapid decline in SFR from $z \sim 1$ to $z \sim 0.3$ (at a fixed stellar mass), with a slope $\alpha \sim 0.7$ at $z \sim 0.5$. Complementary studies at this time by Elbaz et al. (2007) and Daddi et al. (2007) found a similar trend with slopes close to unity at $z \sim 1$ and 2 respectively. Subsequent work showed an anti-correlation between the specific SFR and stellar mass out to $z \sim 2$ which has been termed *downsizing* (Cowie et al. 1996) where the more massive galaxies form at higher redshift (see e.g. Noeske et al. 2007b; Damen et al. 2009a; Rodighiero et al. 2010).

Since then, there have been many investigations of this relationship, using both observations and simulations, with the aim of shedding light on how it connects with the underlying physical processes governing galaxy evolution. Whilst the general trends in the SF-MS from observations seem to agree, the way in which we obtain SFR measurements, coupled with the choice of initial mass function (IMF), the particular star-forming galaxy (SFG) selection criterion, the modelling of star formation histories (SFH) and stellar population synthesis models (SPS), dust attenuation, extinction, photometric redshifts, metallicities, adopted cosmology and incompleteness, can all introduce bias and calibration issues for modelling the SFR-M_* relation accurately (e.g. Salimbeni et al. 2009;

⋆ rwi.johnston@gmail.com

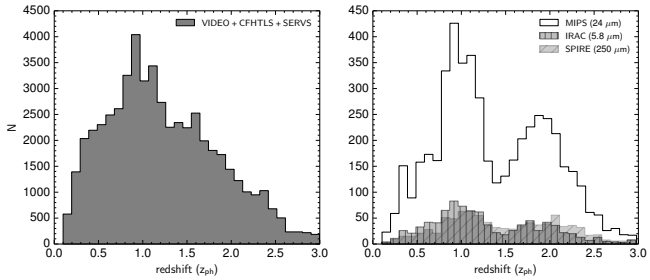

Figure 1. *Left:* The VIDEO redshift distribution from our SERVS-matched sample of 52,812 galaxies. *Right:* The contribution to the redshift distribution by sources detected by MIPS 24 (4881 galaxies), IRAC 5.8 (909 galaxies) and SPIRE 250 μm (901 galaxies).

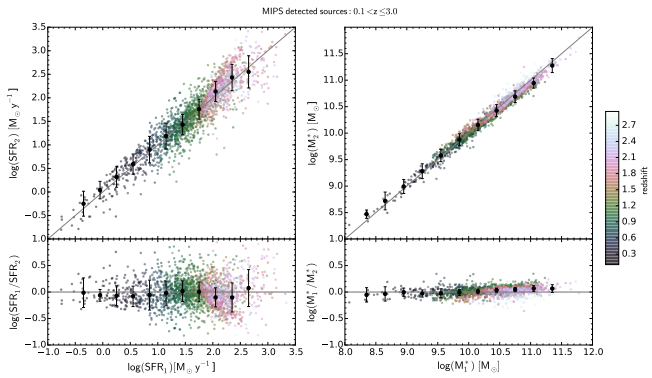

Figure 2. Comparison of the outputs from CIGALE using the full wavelength coverage available and a restricted coverage. The left-hand panels show a comparison of SFR estimates from CIGALE where SFR_1 is the resulting SFR using only the input photometry from VIDEO+CFHT+SERVS. The label SFR_2 is for the same set of objects when we include additional filter information from MIPS+IRAC+*Herschel*. The right-hand panel shows the same comparison for the stellar masses M_1^* and M_2^*. The black points in each panel are the medians with the σ_{MAD} errors. The grey solid lines on the top left and right panels indicates the one-to-one relation. The colour scale indicates increasing redshift from blue to red which covers $0.1 \lesssim z \lesssim 3.0$. The bottom two panels show the $\log_{10}$ of the ratio between SFR_1 and SFR_2 (*left*) and the stellar masses (*right*).

Conroy et al. 2009; Magdis et al. 2010; Walcher et al. 2011; Pforr et al. 2012; Conroy 2013; Buat et al. 2014; Rodighiero et al. 2014; Speagle et al. 2014).

Typical SFR indicators include the UV-wavelength range (e.g. Erb et al. 2006; Magdis et al. 2010; Rodighiero et al. 2011; Lee et al. 2011, 2012) since the emission is dominated by young massive short-lived stars. The UV, however, is heavily affected by extinction and so combining this indicator with IR measurements helps to correct for dust attenuation in the UV which is then re-emitted in the IR and FIR (e.g. Santini et al. 2009; Salmi et al. 2012; Whitaker et al. 2012; Reddy et al. 2012; Smith et al. 2012), or using the IR alone as in e.g. Oliver et al. (2010); Elbaz et al. (2011). Nebula emission lines, e.g. Hα, O[II] and O[III] have also been used (e.g. Chen et al. 2009; Shim et al. 2011; Zahid et al. 2012; Suzuki et al. 2015), as well as from radio continuum emission and stacking techniques (e.g. Dunne et al. 2009; Pannella et al. 2009; Karim et al. 2011; Zwart et al. 2014). Recently, SED modelling algorithms using so-called energy balance methods that exploit the conservation of energy between the stellar light absorbed by dust that is then re-emitted in the mid-IR/far-IR/submm (Burgarella et al. 2005; Noll et al. 2009; da Cunha et al. 2008), have also been used to obtain estimates of the total SFR as well as stellar masses and other physical properties.

All of these approaches have advantages and disadvantages. However, a key issue is the initial selection of SFGs (e.g. Ilbert et al. 2010; Karim et al. 2011). Recent studies by Rodighiero et al. (2014) and Speagle et al. (2014) demonstrate how different colour selection of SFGs leads to large variations in determining the slope of the SF-MS throughout the literature, making direct comparisons challenging.

Nevertheless, some of the most recent work presents evidence for a more complex evolving MS beyond a standard power-law. For example, Heinis et al. (2014); Magnelli et al. (2014); Schreiber et al. (2015) and Whitaker et al. (2014) present results that indicate a MS that flattens off toward the high end of the mass function, favouring a MS modelled by e.g. a broken power-law. In particular, Whitaker et al. (2014), using data from the 3D-HST photometric catalogues and a stacking analysis of MIPS 24μm probed the low mass SF-MS down to $\log_{10}(M_*/M_\odot)$= 8.4 and 9.2, at z=0.5 and 2.5 respectively. From this analysis they parameterised the data with a two-power law model, and found evidence for strong redshift evolution for galaxies with masses $\log_{10}(M_*/M_\odot) > 10.2$. However, they found no evolution for galaxies below this mass limit, suggesting that high-mass SFGs may follow a different evolutionary path than lower mass galaxies. This trend at the high-mass end has also been reported by Tasca et al. (2014) using data from the VIMOS Ultra-Deep Survey (VUDS) at $z \sim 1.5$.

In parallel, over the last decade there have been significant advances in simulations providing insight into galaxy formation through the modelling of physical and environmental processes. The most popular approaches that have emerged are the semi-analytical models (SAMs) and hydrodynamical simulations. SAMs use an analytical approach, requiring up to ~50 parameters to characterise the gas dynamics within and around halos (e.g. Bower et al. 2006; Kitzbichler & White 2007; Bower et al. 2008; Guo & White 2008). Whilst they have been largely successful at reproducing observed SFRs of local populations ($z \lesssim 0.4$), the work by e.g. Elbaz et al. (2007); Daddi et al. (2007); Santini et al. (2009) and Damen et al. (2009b) have shown they consistently under predict the star formation rate by a factor of 2-5 out to $z \sim 2$.

With the advances in computational power, hydrodynamical simulations have grown in popularity. This approach attempts to model the physical dynamics of cosmic gas in a self consistent way by including the modelling of star formation processes, feedback from stellar winds, supernovae, and black holes (e.g. Davé et al. 2011, 2013; Dubois et al. 2014; Vogelsberger et al. 2014; Sparre et al. 2014). However, while there may be broad agreement with overall trends of the SFR-M_* relation with observations, they too exhibit a consistent under prediction in the overall normalisation across most redshifts (e.g. Daddi et al. 2007; Tasca et al. 2014).

In this work we explore the SF-MS, focusing on using CIGALE (Noll et al. 2009), which incorporates empirical relations to build a grid of libraries that model: SFHs using SPS models (e.g. Fioc & Rocca-Volmerange 1997; Bruzual & Charlot 2003; Maraston 2005), interstellar gas and dust (e.g. Calzetti et al. 1994; Calzetti 1997; Dale & Helou 2002), fraction of AGN (e.g. Fritz et al. 2006) and optical and UV interstellar emission and absorption lines (see e.g. Kinney et al. 1996; Noll et al. 2004). We use observations pri-

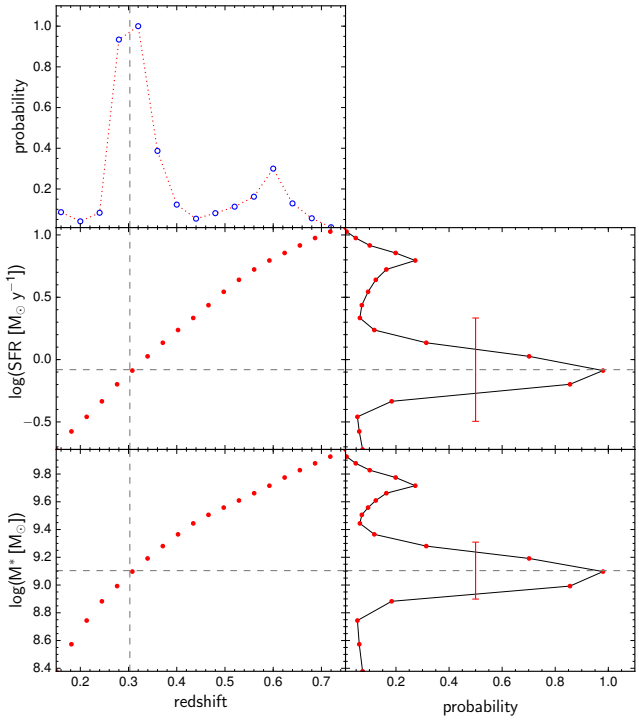

Figure 3. Example illustrating how we propagate photometric redshift PDF estimates through CIGALE. The top panel shows a typical redshift PDF outputted by LEPHARE and the blue open circles represent the gridded redshift steps. The best-fit redshift for this object is shown by the vertical dashed line. To estimate the resulting PDF for the SFR and M_*, we run CIGALE for a series of redshift steps that encapsulate the full range of the z_{ph}-PDF as shown in the middle and bottom panels by the red solid dots. Finally, we weigh the resulting SFR and M_* distributions by the z_{ph}-PDF probabilities and shown in the right-hand middle and bottom panels. For completeness, the horizontal dashed lines denote the resulting CIGALE fitted values for the *best-fit* LEPHARE input redshift value (i.e. a single redshift) with the corresponding CIGALE error estimates on these parameters shown as the vertical red error bars.

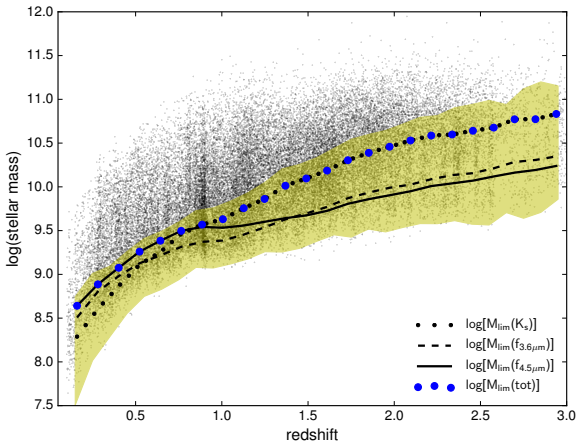

Figure 4. Stellar-mass completeness as a function of redshift.The black dots show the distribution our final sample of 52,812 galaxies. The transparent yellow region shows the stellar-mass limit $M^*_{\rm lim}$, for all objects that could be detected with an apparent magnitude limit of $K_{\rm s} < 23.0$. The black dotted line indicates the mass completeness limit for the $K_{\rm s}$ band. As our sample is jointly selected with IRAC1 and IRAC2 bands at 3.6 and 4.5 μm we compute the mass completeness limits for these bands as shown by the dashed and solid black lines respectively. The blue dots trace our final mass completeness limit which selects the highest mass limit from the three bands.

marily derived from the VISTA Deep Extragalactic Observations (VIDEO) (Jarvis et al. 2013).

The format of this paper is as follows. In § 2 we provide full details of the data and our sample selection followed by a description of the SED fitting code CIGALE in § 3. In this section we also discuss how we can extend this algorithm to account for the full propagation of photometric redshift PDFs and discuss completeness estimates and other sources of uncertainties. In § 4 we discuss the various ways in which we model the SF-MS and then present our results in § 5. In § 6 we compare our observational results to a variety of simulations to investigate how the key physical processes invoked in the simulations to reproduce local relations, effect the SF-MS at $0.5 < z < 3$. A final discussion and conclusions can be found in § 7. Throughout this work we adopt an H$_0$=70 km s^{-1} Mpc^{-1}, Ω_M=0.3, Ω_Λ = 0.7 cosmology.

2 SAMPLE SELECTION

2.1 The VIDEO Survey

For our analysis we use K_s-selected galaxies from the VISTA Deep Extragalactic Observations (VIDEO; Jarvis et al. 2013) Survey. VIDEO is a $\sim$ 12 degree^2 survey in the near-infrared *Z, Y, J, H* and $K_{\rm s}$ bands that has been designed to trace the evolution of galaxies and clusters as a function of both epoch and environment out to $z \sim 4$. VIDEO is being carried out over three of the most widely observed high-Galactic-latitude fields, covering $\sim$3 deg^2 in the ELAIS-S1 field, $\sim$4.5 deg^2 in the XMM-Newton large-scale structure field, and another $\sim$4.5 deg^2 in the extended Chandra Deep Field-South. These fields have a wealth of data from the X-rays through to the radio waveband, and are, along with COSMOS/UltraVISTA, the primary fields for observations with future facilities in the Southern hemisphere.

In this work we focus on an area within the XMM-LSS field where VIDEO observations overlap with the Canada-France-Hawaii-Telescope Legacy Survey Deep 1 (CFHTLS-D1 Ilbert et al. 2006) field, providing optical photometry in the $ugriz$ bands. The creation of the CFHTLS/VIDEO catalogue extracted over the 10 bands ($ugriz$ from CFHTLS and $ZJHK_{\rm s}$ from VIDEO) is described in detail by Jarvis et al. (2013). The current full catalogue contains 431, 949 objects over a $\sim$ 1 deg^2 area.

To determine photometric-redshift (z_{ph}) estimates with VIDEO we used the public code LEPHARE[1] (Ilbert et al. 2006). For more details regarding the LEPHARE settings see Jarvis et al. (2013). As is relevant to this work, LEPHARE outputs a redshift probability distribution function (PDF) for each object, which we propagate in our analysis in deriving SFR and M_* estimates,

For our analysis we adopt a conservative approach and only select objects brighter than a limiting apparent K_s-band magnitude $K_s < 23.0$, which corresponds to > 95 per cent completeness for

[1] http://www.cfht.hawaii.edu/~arnouts/LEPHARE/lephare.html

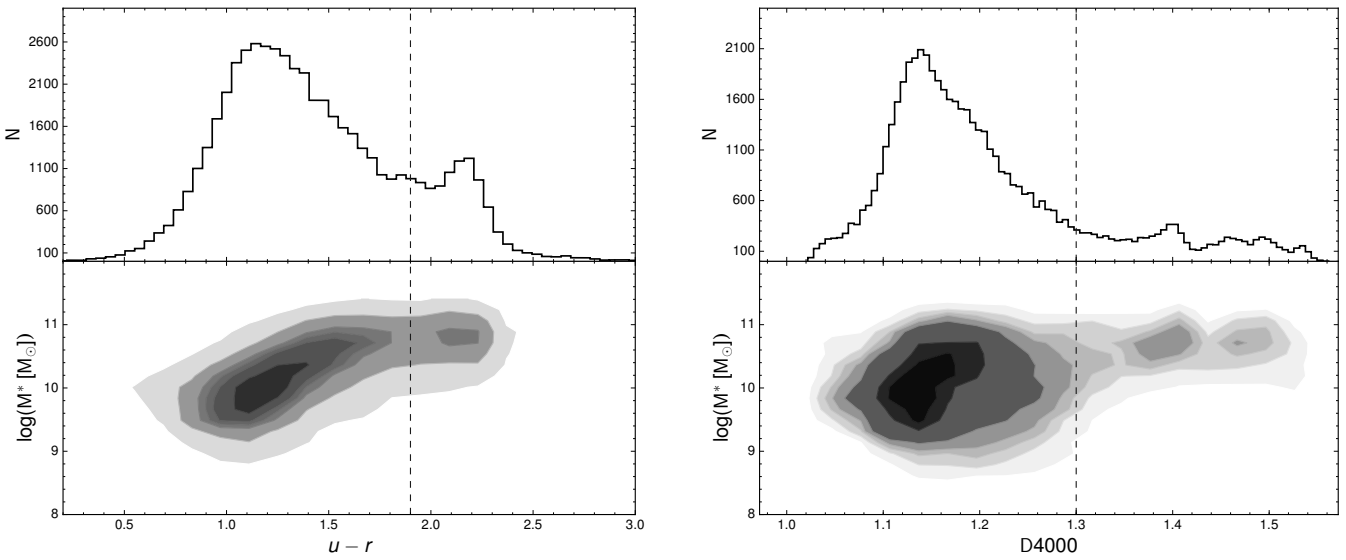

Figure 5. The two methods of selecting SFGs. *Left panel*: the upper plot shows the rest-frame *u-r* colour distribution. The bottom panel shows how this varies as a function of $\log_{10}(M_*/M_\odot)$. The vertical dashed line indicates our colour cut to isolate SFGs; all galaxies with *u-r* > 1.9 are considered to be passive. *Right panel*: the D4000 index as determined by CIGALE. The extended tail in the D4000 distribution shows the residual passive galaxy population that we remove using a cut at D4000=1.3. The bottom panel shows the passive population are mostly massive objects with $\log_{10}(M_*/M_\odot) \gtrsim 10$.

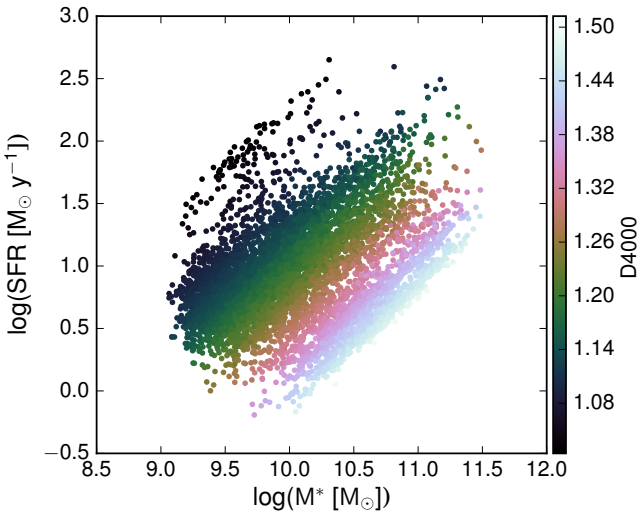

Figure 6. Using the D4000 index to select star forming galaxies as discussed in § 3.3. The colour gradient shows how the D4000 index varies as function of the M_*-SFR distribution for a sample at $z \sim 1$. All parameters were derived from CIGALE.

the VIDEO data (see Jarvis et al. 2013) for $0.1 \leq z_{ph} \leq 3.0$, thus reducing our parent sample to 74,063 galaxies.

2.2 Matching to Multi-wavelength data

The design of the VIDEO survey footprint was driven by the need to cover the wealth of ancillary data available in fields of several square degrees routinely accessible from Paranal. Multi-wavelength observations within VIDEO fields include *Spitzer* (e.g. Lonsdale et al. 2003; Mauduit et al. 2012) and *Herschel* (Oliver et al. 2012), in addition to ongoing ground-based optical surveys from the CFHT, the VLT Survey Telescope (VST[2]) and the Dark Energy Survey (Flaugher 2005; Bernstein et al. 2012). For our analysis we thus built a well-sampled complete multi-wavelength dataset of galaxies detected by VIDEO and matched to available UV-to-IR data.

2.2.1 *SERVS Data*

The Spitzer Extragalactic Representative Volume Survey (SERVS, Mauduit et al. 2012) covers the three VIDEO fields and consists of deep observations in *Spitzer*-IRAC1 and IRAC2 bands at 3.6 and 4.5 μm. We searched for SERVS counterparts to the VIDEO sources within a radius of 1" and only selected objects detected in both bands with fluxes higher than 1.0 μJy (3-σ limit). Our final sample contains 52,812 galaxies. This jointly selected sample at K_s, 3.6 and 4.5 μm ensures that we can reliably detect the emission from the old stellar populations that contribute the bulk of the stellar mass, up to our redshift limit.

2.2.2 *SWIRE and HerMES Data*

The *Spitzer* Wide-Area Extragalactic (SWIRE Lonsdale et al. 2003) survey provides IRAC 5.8 and 8.0 μm and MIPS 24, 70 and 160 μm data over the whole of the VIDEO footprint. For SWIRE, we used the *Spitzer* Data Fusion (Vaccari et al. 2010[3]) catalogues and matched SERVS and SWIRE positions within a search radius of 1".

Far-infrared data was obtained from the HERschel Multi-tiered Extragalactic Survey (HerMES; Oliver et al. 2012) carried out with the SPIRE (Griffin et al. 2010) instrument onboard the *Herschel Space Observatory* (Pilbratt et al. 2010) at 250, 350 and

[2] http://www.mattiavaccari.net/voice/
[3] http://www.mattiavaccari.net/df/

500 μm. The SPIRE source extraction is based on forced photometry at the IRAC positions of 24 μm sources as described in Roseboom et al. (2010), and using an input catalogue based on the *Spitzer* Data Fusion. As with the SWIRE data we match the Roseboom et al. (2010) catalogue to our VIDEO-SERVS objects within 1 arcsec.

3 ESTIMATING *SFR* AND *MASS* WITH CIGALE

To estimate SFRs and M_* we use the public SED fitting code, *C*ode *I*nvestigating *GAL*axy *E*mission, (CIGALE[4]; Burgarella et al. 2005; Noll et al. 2009; Giovannoli et al. 2011), which is optimised to provide physical information of galaxies by fitting their UV-to-IR SEDs. In this section we summarise the main steps of the algorithm.

CIGALE is based on the use of a UV-optical stellar SED plus an IR-emitting, dust component. In essence, CIGALE builds UV-to-IR models which are then fitted to the observed SEDs. The code fits the observed data in the UV, optical, and NIR with models generated with a stellar populations synthesis code, assuming a star formation history (SFH) and a dust attenuation as input. The energetic balance between dust-enshrouded stellar emission and re-emission in the IR is conserved by combining the UV/optical and IR SEDs.

In our implementation, we have used the stellar population synthesis models of Maraston (2005) (hereafter M05) which consider the thermally pulsating asymptotic giant branch (TP-AGB) stars, and use the Kroupa (2001) initial mass function (IMF). We generate star formation histories (SFH) based on two stellar populations: a recent stellar population with a constant SFR on top of an older stellar population created with an exponentially declining SFR. Model spectra are then reddened using attenuation curves from Calzetti et al. (2000), and we use the semi-empirical one-parameter models of Dale & Helou (2002) (hereafter DH02) to fit the stellar-heated dust emission. The DH02 library is composed of 64 templates parametrised by α, the power-law slope of the dust mass over heating intensity. α is directly related to the $f_{60\mu m}/f_{100\mu m}$ flux ratio, where $f_{60\mu m}$ and $f_{100\mu m}$ represent fluxes at 60 and 100 μm, respectively. CIGALE allows us to estimate the fraction of $L_{\rm IR}$ due to an AGN by combining AGN with the starburst templates. We used the set of six templates from the Fritz et al. (2006) library. The final part of this process uses the Kinney et al. (1996) and Noll et al. (2004) spectra to create empirical templates to consider the UV and optical interstellar emission and absorption lines respectively. The SFRs are computed as

$$\mathrm{SFR} = \frac{M_{\rm gal}}{\tau(e^{t/\tau}-1)}, \quad (1)$$

where $M_{\rm gal}$ is the galaxy mass, τ is the e-folding (or decay) time and t is the look-back time. Finally, the physical parameter values corresponding to the best-fit model are constrained via a χ^2 minimisation.

We explore the impact of the CIGALE outputs when flux information is unavailable in certain filters for a given galaxy. The fraction of objects in our sample that were detected in IRAC 3 & 4, MIPS and SPIRE is quite small. Thus, the dominating contributing filters used in CIGALE are from VIDEO, CFHT and SERVS. For this test we have isolated those galaxies that have detections across the entire filter set. We then run CIGALE twice; first with input photometry from *only* VIDEO, CFHT and SERVS, and secondly where we add the additional information from IRAC 3 & 4, MIPS and SPIRE. Figure 2 shows the comparison between the estimated SFR and M_* from CIGALE under these two scenarios. For the comparison of SFRs, we find very good agreement between the outputs, with an average overall scatter in the residuals of $\sigma_M = 0.22$ dex. Similarly for M_* we find a very tight correlation with an average scatter of just $\sigma_M = 0.07$ dex in the residuals. We therefore conclude that CIGALE can robustly estimate the SFR and M_* without the need for the far-IR data to the redshift limit of our sample.

[4] http://cigale.lam.fr/

Table 1. Input parameter for propagating the z_{ph} PDFs through CIGALE. The first column shows the range of ages for the stellar population (SP) models used to create star formation histories. The second column shows the redshift range we permit based on the SP ages.

Ages of old SP models τ_f (Gyr)	Data z-range (best-fit z_{ph})	z-step coverage (CIGALE model range)
5, 6, 7, 8, 9	$0.1 < z \leq 0.3$	$0.01 < z_{step} < 0.41$
2.5, 3.5, 4.5, 5.5, 6.5	$0.3 < z \leq 0.6$	$0.15 < z_{step} < 0.75$
1, 2, 3, 4, 5	$0.6 < z \leq 1.0$	$0.45 < z_{step} < 1.15$
1, 2, 3, 4	$1.0 < z \leq 1.4$	$0.85 < z_{step} < 1.55$
1, 1.5, 2, 2.5, 3	$1.4 < z \leq 2.0$	$1.25 < z_{step} < 2.15$
1, 1.5, 2, 2.5	$2.0 < z \leq 2.4$	$1.85 < z_{step} < 2.55$
1.0, 1.2, 1.5, 1.7,1.9	$2.4 < z \leq 3.0$	$2.25 < z_{step} < 3.15$

3.1 Propagating the z_{ph} uncertainties through CIGALE

CIGALE requires the redshift of the galaxy as input and is not currently optimised to simultaneously constrain redshift *and* physical properties of the galaxies. We therefore modified CIGALE to obtain both SFR and M_* estimates when we have the full photometric redshift PDF. For our sample such information was obtained from LEPHARE and propagating this through the CIGALE framework required only a slight modification.

This modification is illustrated in Figure 3. The top panel shows a typical redshift PDF outputted from LEPHARE, where the blue circles represent the resolution of the LEPHARE grid for a given galaxy. As we can see in this example, there are two peaks in the z_{ph}-PDF; the first at $z\sim0.3$ and the second at $z\sim0.6$ with a lower probability. The majority of the contribution is centred at $z\sim0.3$ and LEPHARE returns a best-fit value as indicated by the vertical dashed line. To include the full z_{ph} contribution for a given galaxy we run CIGALE at a series of redshift steps that cover the range that fully describes the z_{ph}-PDF. The middle and bottom left-hand panels in Figure 3 show the resulting $\log_{10}$(SFR) and $\log_{10}(M_*)$ estimates from CIGALE respectively as a function of redshift. Finally, we can weight this relation in SFR and M_* according to the interpolated probability distribution of the z_{ph}, as shown in the right-hand bottom and middle panels. We also show the estimated error on the SFR and M_* from CIGALE for this galaxy using the best-fit redshift value.

To account for the range in the full photometric redshift PDF estimation from LEPHARE, we ran CIGALE with different stellar population (SP) model ranges according to a set of redshift slices which are summarised in Table 1. The use of applying two stellar populations was explored in more detail recently by Buat et al. (2014), who applied a similar approach to derive SFRs and M_* estimates at redshifts $z > 1$. Our approach allows for z_{ph}-PDFs that may not be well described by e.g a simple gaussian. In § 5 we apply this approach in determining SF-MS.

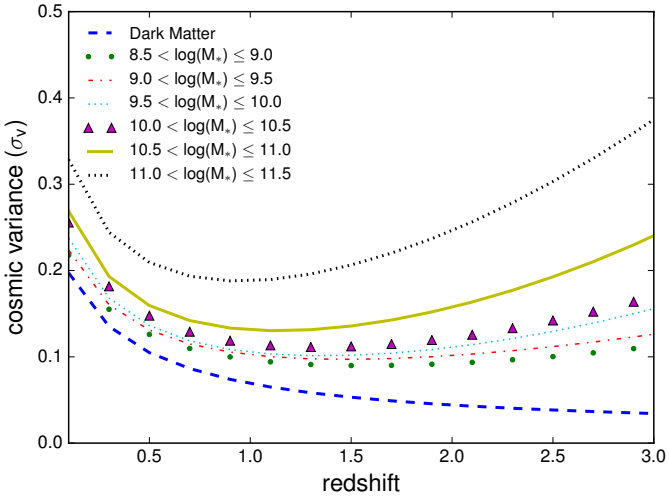

Figure 7. Cosmic variance as a function of redshift for a range of mass bins for the current VIDEO data release covering 1 deg^2.

3.2 Stellar mass completeness

To estimate the completeness limit for M_* we follow the approach used by Ilbert et al. (2013) and Pozzetti et al. (2010), and which is illustrated in Figure 4, where we show the stellar masses for our sample of 52,812 galaxies as a function of redshift. We calculate the lowest stellar mass which could be detected for a given galaxy with

$$\log_{10}(M_{\rm lim}) = \log_{10}(M_*) + 0.4(K_{\rm s} - K_{\rm s}^{\rm lim}), \quad (2)$$

where, in our study, the apparent magnitude limit, $K_{\rm s}^{\rm lim} = 23.0$. This is shown as the transparent yellow region on Figure 4. We then bin the data in redshift and compute the 90th percentile of stellar mass within each bin, shown as blue dots in the figure. Thus for a given redshift, we can interpolate the stellar mass completeness limit that corresponds to the mass for which 90 per cent of galaxies fall below the percentile.

3.3 Selecting star-forming galaxies

To analyse the SF-MS we need to isolate SFGs and remove any passive galaxies that would contaminate the sample. However, selecting SFGs from multi-wavelength data can be done in a variety of ways. This was recently reviewed by Speagle et al. (2014) and explored in detail by Rodighiero et al. (2014), where they highlighted how different colour selections can lead to different SFG populations being isolated, contributing to the broad range of derived slopes in the literature. For example, applying a BzK selection (e.g. Daddi et al. 2004; Rodighiero et al. 2011; Kashino et al. 2013) tends to isolate more active SFGs, biasing against galaxies which would otherwise be classified as SF by other methods (e.g. NUVrJ). This type of selection generally leads to steeper derived slopes for the SF-MS. To help avoid selecting only the bluest most active galaxies, Ilbert et al. (2013) used a mixed approach and applied two colour selections in $r - J$ and NUV-r, which provided a broader range of SFGs. In a recent paper by Renzini & Peng (2015) they suggest a construction of a 3D SFR-Mass-Number distribution may help in defining a more objective SF-MS by adopting a cut at the ridge line of the star-forming peak.

In this study we explored two approaches which yielded very different results in our final analysis. With the filter coverage available to us we found a rest-frame *u-r* was the optimal colour selection approach, but not necessarily the most effective way to remove the passive population. The top-left panel of Figure 5 shows the *u-r* distribution where we observe a bimodal distribution, split approximately at *u-r* ~ 1.9, as indicated by the vertical dashed line. The bottom-left panel shows the *u-r* as function of stellar mass (as determined using CIGALE) which perhaps better illustrates this segregation in the two populations. As such we removed all objects in our final sample with *u-r* > 1.9. However, as we shall discuss in the § 5, this does lead to a significant fraction of passive galaxies being missed, along with potential SFGs being removed from the sample at redshifts $z \lesssim 1$.

Alternatively, one may use the 4000 Å break (hereafter referred to as D4000). The D4000 index provides useful information regarding the age of the stellar population and perhaps provides a more physical selection process. A low index indicates a young stellar population, whereas the larger the value the older the galaxies (e.g. Kauffmann et al. 2003; Westra et al. 2010). We use CIGALE to determine the D4000 index as part of the fitting procedure, adopting the definition as detailed in Balogh et al. (1999). Moreover, the calculation is intrinsically a dust-free measurement, as it is based on the unreddened spectra. Whilst this approach is SED-model dependant, it does provide us with a self-consistent approach to identify SFGs. In the right-hand panel of Figure 5 we show the resulting D4000 distribution as a function of M_*. We apply a conservative cut at D4000 = 1.3, and consider galaxies beyond this limit to be older passive galaxies. For the remainder of this article our results will be based on this D4000 selection. As we can see in Figure 6 this type of selection imposes a much sharper cut in the SFR-M_* plane as a function of redshift impacting on conclusions drawn about the evolution of the SF-MS as we will discuss in more detail in § 5.4.

4 MODELLING THE SF-MS

We parameterise and model the SF-MS in a number of ways to test the robustness of our findings and to allow direct comparison with a number of related works. The most common approach is to assume a simple power-law of the form

$$\log_{10}({\rm SFR}) = \alpha \log_{10}(M_*) + \beta, \quad (3)$$

(see e.g. Noeske et al. 2007a; Daddi et al. 2007; Elbaz et al. 2007; Santini et al. 2009; Heinis et al. 2014). Without a redshift dependent term, the data can be simply split into a series of redshift slices, and a fit is perfomed within each slice to determine how the normalisation β and the slope α of the SF-MS evolve.

We calculate the total error on the median SFRs in each bin as $\sigma_{\rm tot}$=$\sqrt{(\sigma_{\rm MAD}^2 + \sigma_{\rm V}^2)}$, where $\sigma_{\rm MAD}$ is the error on the median (median absolute deviation, or MAD), and is related to the standard error on the mean σ by $\sigma < x > = \sigma\bar{x}/1.4826$ (Hoaglin et al. 1983). This is combined in quadrature with the cosmic variance uncertainty $\sigma_{\rm V}$. This is the uncertainty in observed number density of galaxies arising from the underlying large-scale density fluctuations. We have used the public code GETCV developed by Moster et al. (2011), to estimate cosmic variance as a function of redshift for the range in M_* considered. Figure 7 shows how the fractional cosmic variance error $\sigma_{\rm V}$ varies as a function of redshift for a range of stellar mass bins as computed for our sample. We then perform a least-squares fit to estimate the power-law parameters in Equation 3.

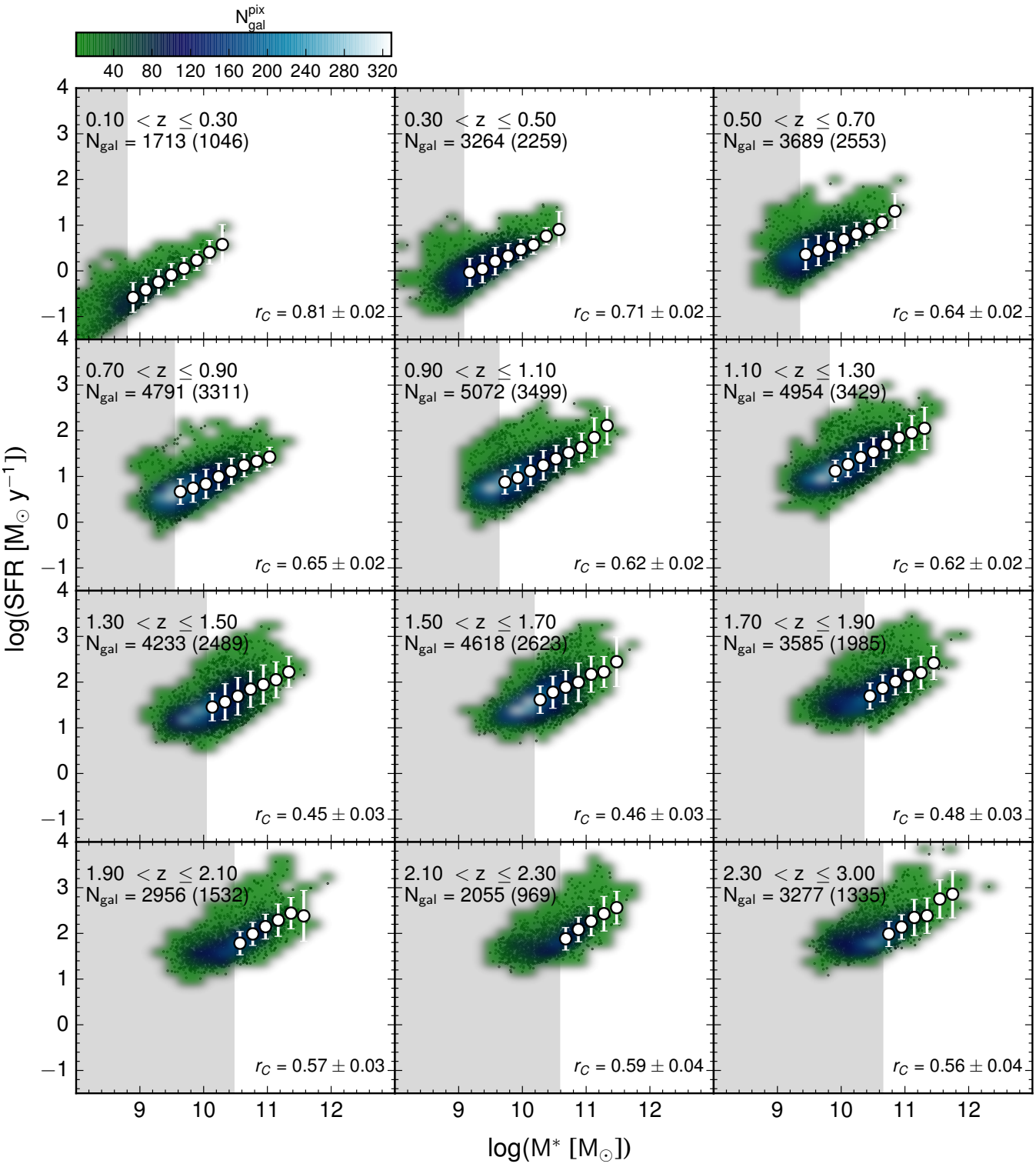

Figure 8. The SF-MS for SFGs from $0.1 < z < 3.0$. The coloured regions are a 2D histogram of the SFR-M_* distribution, where the number of objects in each pixel (δSFR $= \delta M_*$= 0.2) is indicated in the colour bar at the top of the figure ($N_{\rm gal}^{\rm pix}$). The white filled circles denote the median values with their respective uncertainties computed as $\sigma_{\rm tot}$=$\sqrt{(\sigma_{\rm MAD}^2 + \sigma_{\rm V}^2)}$ which combines the mean absolute deviation and cosmic variance (see text for details). The grey area shows the region of our stellar mass completeness limit. Any data within this region is not considered in the final analysis. $N_{\rm gal}$ indicates the total number of galaxies in each panel, with the total number within our stellar mass completeness range shown in parenthesis. The correlation coefficient between SFR and M_* for the stellar mass-complete data is shown as r_c in each panel.

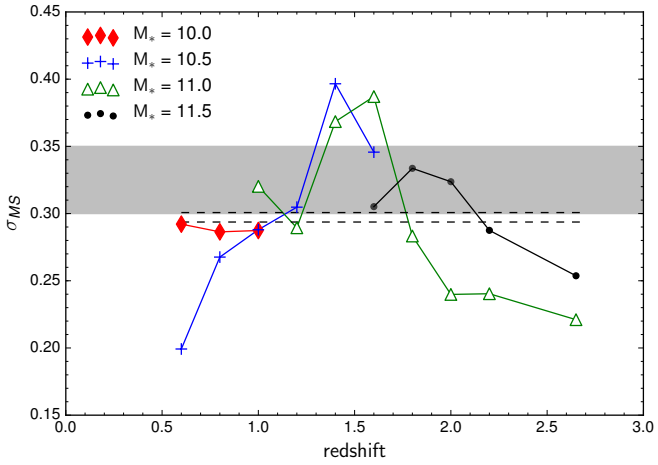

Figure 9. The dispersion in the SF-MS, σ_{MS}, as a function of redshift for a series of stellar-mass bins. The grey shaded region shows a range of σ_{MS} as reported in e.g. Noeske et al. (2007b); Whitaker et al. (2012) and Magnelli et al. (2014). The region between the dashed line indicates our average dispersions across all stellar mass bins where for $\log_{10}(M_*/M_\odot)$=10.0, 10.5, 11.0 and 11.5, $\bar{\sigma}_{MS}$= 0.29, 0.29, 0.31 and 0.28 respectively as estimated within the stellar mass completeness limits.

Although using the median SFR can be useful when dealing with a statistically-small sample, it naturally leads to a loss of information. Therefore, we also perform power-law fits within each redshift slice to the *full* galaxy distribution which we refer to as 'all-data' fits and consider the uncertainty on the SFR and M_* for each individual galaxy as determined using CIGALE.

Recent studies by e.g. Magnelli et al. (2014); Whitaker et al. (2014); Schreiber et al. (2015) and Tasca et al. (2014) have found a flattening of the MS towards the high mass end, and therefore require more robust modelling using either e.g. a broken power-law or an extra term in the form of a quadratic given by

$$\log_{10}(\mathrm{SFR}) = \mathrm{A}_1 + \mathrm{A}_2\log_{10}(\mathrm{M}_*) + \mathrm{A}_3[\log_{10}(\mathrm{M}_*)]^2. \quad (4)$$

Others have instead chosen to model the SF-MS jointly with a redshift-evolution term. In Schreiber et al. (2015) they parameterise as

$$\log_{10}[\mathrm{SFR}(z)] = \log_{10}(M_*) - \alpha_1 + \beta_1\log_{10}(1+z) - \beta_2[\max(0, \log_{10}(M_*) - \alpha_3\log_{10}(1+z)]^2 \quad (5)$$

Alternatively, Whitaker et al. (2012), applied a second order polynomial of the form

$$\log_{10}[\mathrm{SFR}(z)] = \alpha(z)[\log_{10}(M_*) - 10.5] + \beta(z), \quad (6)$$

where the terms $\alpha(z)$, $\beta(z)$ are given by,

$\alpha(z) = \alpha_1 + \alpha_2 z$, and

$\beta(z) = \beta_1 + \beta_2 z + \beta_3 z^2$,

and α_1, α_2, β_1, β_2 and β_3 are the fitting parameters. To explore evolution we adopt the Whitaker et al. (2012) form, applying our z_{ph}-PDF approach as detailed in § 3.1. In practice we create 1000 Monte Carlo (MC) samples randomly drawn from these PDFs, which are then individually fitted via Monte Carlo Markov Chain (MCMC). We can then examine the distribution of parameter constraints to assess any bias from the standard fitting procedure. We have used the public MCMC algorithm CosmoMC (Lewis & Bridle 2002). Samples are generated using the Metropolis–Hastings algorithm (Hastings 1970) for each of several intercommunicating Markov chains, with a 'proposal distribution function' that allows full exploration of the posterior space. We adopt a χ^2 likelihood given by

$$-2\log_{10}(\mathcal{L}) \equiv \chi^2 = \sum_{i=1}^{N} \frac{[\log_{10}(\mathrm{SFR_i^{data}}) - \log_{10}(\mathrm{SFR_i^{mod}})]^2}{\sigma^2_{\mathrm{tot,i}}}. \quad (7)$$

where $\log_{10}(\mathrm{SFR}_i^{\mathrm{data}})$ is the observed data and $\log_{10}(\mathrm{SFR}_i^{\mathrm{mod}})$ is the model. We apply this model to our z_{ph}-PDF analysis of the SF-MS and our σ_{tot} in this case includes the intrinsic dispersion of the SFR-z and M_*-z distributions as well as σ_{V} giving $\sigma_{\mathrm{tot}}(z)$=$\sqrt{[\sigma_{M_*}(z)^2 + \sigma_{\mathrm{SFR}}(z)^2 + \sigma_V^2]}$.

4.1 Calibration of the main-sequence

In § 5.2 we compare our SF-MS results to a range of recent studies. However, as we can see from Table 2 there is a spread in the underlying assumptions to determining stellar masses and SFRs that include: wavelength coverage/selection of an observed sample, SFR estimation (L − SFR relation), the IMF, stellar population synthesis models (SPS), extinction, metallicities, adopted cosmology, not to mention other contributing factors such as the modelling star formation histories (SFH), dust attenuation, photometric redshifts and incompleteness. Whilst for any given study the results may be self consistent, quantifying differences in the SF-MS beyond their intrinsic scatter due to differing assumptions can be challenging. In general, calibration of MS data is typically an average correction which impacts the normalisation. In an attempt to make a fair comparison we have adopted a similar calibration approach detailed in Speagle et al. (2014) (S14). In their study they examined twenty-five recent studies and highlight three major sources that require a calibration offset, namely the choice of IMF, SFR indicators (L − SFR relation) and SPS modelling. For the works that overlap with ours in Table 2 we have used the S14 re-calibrated MS power-law fits which we show in Table 4. Whilst S14 estimate offsets for e.g. adopted cosmology, extinction, emission line, these were shown to be sub-dominant to the IMF, SPS models and SFR indicators. As such, in our calibration we consider only contributions from the latter.

The IMF offsets used in S14 were taken from taken from Zahid et al. (2012) where they calibrated to the Kroupa IMF using

$$M_*^K = 1.06M_*^C = 0.62M_*^S, \quad (8)$$

where the superscripts refer to Kroupa, Chabrier (Chabrier 2003), and Salpeter (Salpeter 1955) IMFs, respectively. As they calibrate to the Kroupa IMF, these would lead to respective offsets in stellar mass for Chabrier and Salpeter of $C^C_{M_*}$ = +0.03 and $C^S_{M_*}$ = -0.21. This would translate to an offset in the normalisation of the MS fit by

$$\beta_C = \beta_0 - \alpha \times C_{M_*}, \quad (9)$$

where β_C is the calibrated normalisation, β_0 is the original fitted normalisation and α is the slope. Since we have applied the Kroupa IMF in our analysis we do not include this offset in our calibration.

There have been a number of investigations into the differing approaches to generating SPS models and in particular the treatment of the modelling of thermally pulsating asymptotic giant branch (TP-AGB) stars. (e.g. Salimbeni et al. 2009; Conroy et al. 2009; Magdis et al. 2010; Walcher et al. 2011). To calibrate

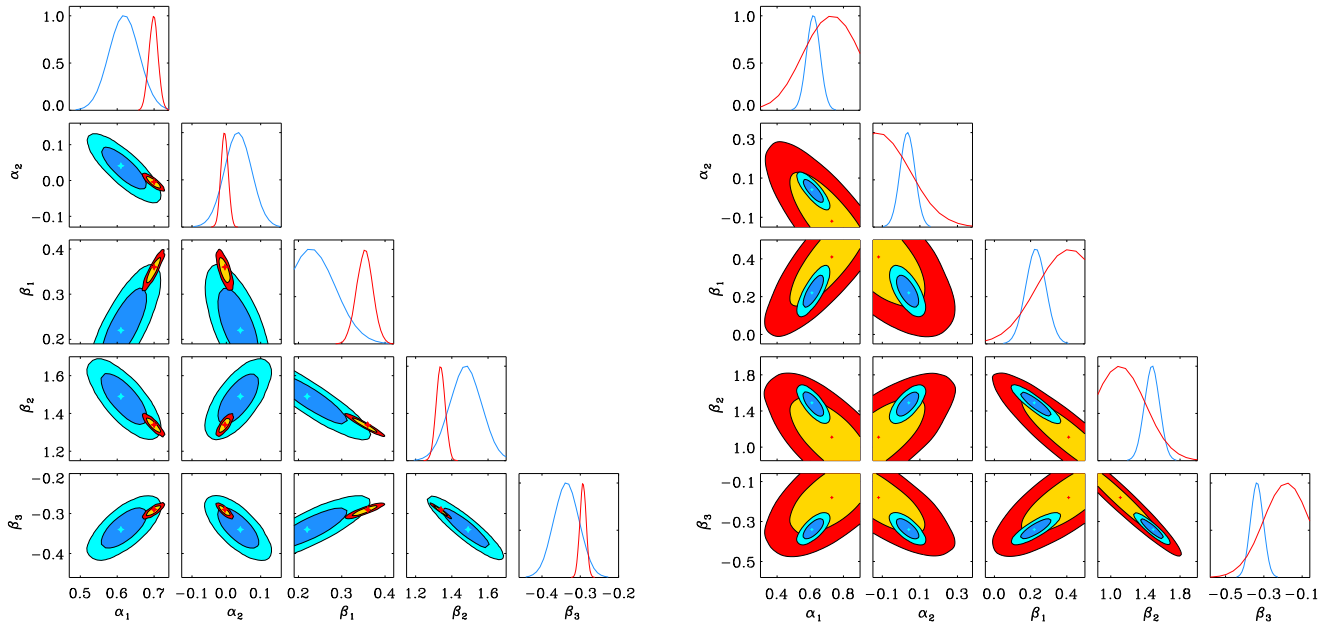

Figure 10. Parameter constraints from our MCMC analysis of the model shown in Equation 6. *left panel set:* The dark and light blue shaded contours show the 2-D 1σ and 2σ marginalised results respectively. The red and yellow contour regions show an example from the 1000 Monte Carlo z_{ph}-PDF constraints. The 1-D marginalised probability distributions are shown on the diagonal as the blue line (red line) for the VIDEO median (z_{ph}-PDF) fits. The cross near the centre of each contour set shows the best-fit parameter value. *right panel set:* Comparison of Whitaker et al. (2012) median fits (red and yellow shaded contours) with our median fits (blue contours).

from M05 to BC03 (as in S14) we adopt the conservative offset of $C^{SPS}_{M_*}$= +0.15 dex which was an estimated average from analyses from Magdis et al. (2010); Salimbeni et al. (2009); Conroy et al. (2009). Therefore, we apply Equation 9 to obtain the MS offset.

In a recent study by Buat et al. (2014) they examined potential SFR offsets derived from CIGALE compared to that of a standard $L-$SFR relation that convert FUV and IR luminosities in to SFRs, and found a very tight correlation with that of the CIGALE derived SFRs. In the case of the two population model, which we have applied in our analysis, they reported a small offset resulting in a slight underestimate of the instantaneous SFR with $\mathrm{SFR_{IR,FUV}}$. For our analysis we therefore do not attempt a correction, but intend to investigate this more deeply in subsequent work.

To summarise, we have found that our dominant source of calibration required for our comparison is from the SPS models. Our total calibration offsets in the normalisation of our 'raw' MS fits can be found on Table 4.1 (shown in parenthesis) along with the S14 derived offsets for the works we compare to in Table 2.

5 RESULTS

Figure 8 shows the SF-MS for our SFG sample across twelve redshift bins. The grey region in each panel shows the M_* completeness limit; galaxies within this region are excluded from our analysis. The blue and white circles show the median SFRs in bins of width ΔM_* = 0.2 dex.

We find a consistent correlation between SFR and M_* out to $z < 3.0$ which we quantify with the correlation coefficient, r_c, in each redshift panel on the Figure. We find an average value of $r_c = 0.61$; a trend consistent with many other works (e.g. Erb et al. 2006; Daddi et al. 2007; Noeske et al. 2007b; Dunne et al. 2009; Pannella et al. 2009; Rodighiero et al. 2010; Elbaz et al. 2011; Whitaker et al. 2012; Muzzin et al. 2013; Magnelli et al. 2014). We have also estimated the dispersion of the SF-MS denoted as σ_{MS} in Figure 9, for four stellar mass bins with $\Delta\log_{10}(M_*/M_\odot)$ = 0.5 dex, centred on $\log_{10}(M_*/M_\odot)$= 10.0 (red), 10.5 (blue), 11.0 (green) and 11.5 (black). Previous studies by e.g. Noeske et al. (2007b); Whitaker et al. (2012) and Magnelli et al. (2014) have reported an average dispersion over all stellar mass ranges between $\sim$0.3 and 0.35, which is indicated by the shaded grey region in Figure 9. As we can see, our values for σ_{MS} vary about this region as a function of redshift, where in general at $z \lesssim 1.4$ we find $0.27 < \sigma_{MS} < 0.32$, at $1.4 < z < 1.6$ the scatter increases to $\sigma_{MS} \sim 0.38$ before showing an overall decline towards $z \sim 3$ for the highest stellar mass bins with $\log_{10}(M_*/M_\odot)$=11.0 and 11.5. This decline in dispersion was also alluded to in Whitaker et al. (2012) and Daddi et al. (2007). If we take the average values of σ_{MS} for each stellar mass bin across their respective redshift ranges we find for $\log_{10}(M_*/M_\odot)$=10.0, 10.5, 11.0 and 11.5 dispersions of $\bar{\sigma}_{MS}$= 0.29, 0.29, 0.31 and 0.28 respectively.

5.1 Main Sequence constraints - I

In this section we model the SF-MS relation using the redshift-dependent model given by Equation 6 and to check the robustness of our results we model our data with three approaches. In the first we explore the contribution from our z_{ph}-PDF derived values for SFR and M_* as detailed in § 3.1. We then model our observed full sample that includes intrinsic errors from CIGALE and finally fit to the median values of Figure 8 which allows a more direct comparison to the work of W12. Table 3 summarises the results of these fits.

In the second column in Table 3 we account for each LEPHARE z_{ph}-PDF by creating a set of 1,000 Monte Carlo (MC) data-sets by

Table 2. Details of the properties of the various constraints we compared to in Figure 12. Column 2: the initial mass function (IMF) used, column 3 is the indicator used estimate SFRs, column 4: wavelength selection of the parent sample, column 5: method to select star-forming galaxies, column 6: stellar population synthesis (SPS) model used, column 7: extinction law, column 8: adopted cosmology, column 9: survey and column 10: total area of sample.

Source	IMF	SFR Indicator	Wavelength selection	SFG selection	SP Model	Extinction Law	Cosmology $(h, \Omega_m, \Omega_\Lambda)$	Survey	Area deg^2
This work	Kroupa	SED (CIGALE)	K/3.6, 4.5 μm	D4000, u-r	M05	[d]C00	(0.7,0.3,0.7)	VIDEO/CFHT/SERVS	1
Daddi et al. (2007)	Salpeter	Hα	K	$sBzK$	BC03	[e]P84	(0.7,0.3,0.7)	GOODS	0.033
Dunne et al. (2009)	Salpeter	1.4 GHz	K	None	BC03	C00	(0.71,0.27,0.73)	UDS/UKIDSS	0.8
Elbaz et al. (2007)	Salpeter	Hα	UV/opt	blue	[a]PEGASE.2	[f]CF00	(0.7,0.3,0.7)	SDSS/GOODS	705
Elbaz et al. (2011)	Salpeter	FUV	FIR	blue	PEGASE.2	C00	(0.7,0.3,0.7)	GOALS/AKARI/SDSS	38960
Heinis et al. (2014)	Chabrier	UV+IR	UV	None	BC03	None	(0.7,0.3,0.7)	HerMES/COSMOS	1.68
Magnelli et al. (2014)	Chabrier	UV+IR	K	3σ-clip	BC03	None	(0.71,0.27,0.73)	COSMOS	1.97
Noeske et al. (2007b)	Kroupa	UV+IR	Optical	redshift	BC03	[g]CE01	(0.7,0.3,0.7)	AEGIS	1
Oliver et al. (2010)	Salpeter	IR	FIR	None	[b]R08	None	(0.7,0.3,0.7)	SWIRE	11.33
Pannella et al. (2009)	Salpeter	1.4 GHz	$sBzK$	$sBzK$	BC03	P84	(0.7,0.3,0.7)	COSMOS	0.9
Reddy et al. (2012)	Salpeter	UV+IR	UV	LBG	[c]CB11	C00	(0.7,0.3,0.7)	various	0.081
Rodighiero et al. (2010)	Salpeter	UV+IR	4.5 μm	U-B	BC03	C00	(0.7,0.27,0.73)	GOODS	?
Rodighiero et al. (2011)	Salpeter	UV+IR	NIR+FIR	$sBzK$	BC03	C00	(0.73,0.26,0.74)	COSMOS/GOODS-MUSIC	1.73
Santini et al. (2009)	Salpeter	UV+IR	z/K/4.5 μm	2σ-clip	M05	C97/C00	(0.7,0.3,0.7)	GOODS-MUSIC	0.04
Schreiber et al. (2015)	Salpeter	UV+IR	H/K	UVJ	BC03	C00	(0.7,0.3,0.7)	CANDELS-GOODS/COSMOS	1.8
Whitaker et al. (2012)	Kroupa	UV+IR	NIR	UVJ	BC03	C00	(0.7,0.3,0.7)	NMBS	0.4
Whitaker et al. (2014)	Chabrier	UV+IR/Hβ	NIR	UVJ	BC03	C00	(0.7,0.3,0.7)	CANDELS/3D-HST	0.25
Zahid et al. (2012)	Chabrier	Hα/Hβ	Optical/UV	Lines	BC03	C00	(0.7,0.3,0.7)	SDSS-DR7/DEEP2	0.5

[a] Fioc & Rocca-Volmerange (1997), [b] Rowan-Robinson et al. (2008), [c] Charlot & Bruzual (2011) (never formally published)
[d] Calzetti et al. (2000), [e] Prevot et al. (1984), [f] Charlot & Fall (2000), [g] Chary & Elbaz (2001)

Table 3. SFR-MS parameterised according to Equation 6. The second column shows the results when we propagate the full redshift PDFs through CIGALE, computed as the mean of the 1000 Monte Carlos fits with their respective averaged 1σ standard deviations. The third column is fitted to the full observed data-set including the intrinsic errors on stellar mass and SFR from CIGALE ($\sigma^2_{\rm cig}$), the uncertainty on the best-fit redshift from LEPHARE ($\sigma^2_{\rm leph}$), the intrinsic dispersion of the SFR and stellar mass distributions ($\sigma^2_{\rm disp}$), and finally the uncertainty due to cosmic variance ${\sigma_{\rm V}}^2$. The forth column shows our fits to the median values and the last column shows the fits to the median values from Whitaker et al. (2012). The reduced χ^2/ν is shown in the bottom row.

	This Work $(0.1 < z_{ph} \leq 3.0)$			Whitaker et al. (2012) $(0 < z < 2.5)$
Parameter (Equ. 6)	z_{ph}-PDF (all data)	$[\sigma^2_{\rm cig}+\sigma^2_{\rm leph}+\sigma^2_{\rm disp}+{\sigma_{\rm V}}^2]$	(medians)	(medians)
α_1	0.68 $\pm$ 0.01	0.68 $\pm$ 0.01	0.62 $\pm$ 0.04	0.73 $\pm$ 0.16
α_2	0.004 $\pm$ 0.011	0.004 $\pm$ 0.011	0.03 $\pm$ 0.04	-0.12 $\pm$ 0.16
β_1	0.33 $\pm$ 0.02	0.29 $\pm$ 0.02	0.24 $\pm$ 0.05	0.41 $\pm$ 0.17
β_2	1.36 $\pm$ 0.03	1.45 $\pm$ 0.03	1.47 $\pm$ 0.08	1.11 $\pm$ 0.28
β_3	-0.30 $\pm$ 0.01	-0.32 $\pm$ 0.01	-0.33 $\pm$ 0.03	-0.18 $\pm$ 0.11
χ^2/ν	0.70	0.78	0.49	0.05

randomly sampling from the PDFs and generating corresponding SFRs and stellar masses as described in § 3.1. We then fit Equation 6 to each MC sample where the likelihood term includes an additional uncertainty for the intrinsic dispersions of SFR-z and M_*-z distributions as well as the contribution from cosmic variance $\sigma_{\rm V}$. In this way we can directly inspect the distribution of constrained parameters and estimate their confidence limits. Here, the marginalised parameter constraints are the mean of the 1000 MC sample distributions and the associated errors are the mean 1σ standard deviations. In the third column of the table we fit Equation 6 to our actual observed sample to incorporate statistical uncertainties from the intrinsic errors from CIGALE on SFR and M_* the uncertainty on the best-fit redshift from LEPHARE, the intrinsic dispersion of the SFR-z and M_*-z distributions, and the uncertainty due to cosmic variance. Our median results are then shown in the fourth column with the W12 constraints presented in the last column of the table. It should be noted that we have reanalysed their median data points using the MCMC routine to provide error estimates on the parameters that were not previously available.

In the left hand panel of Figure 10 we show an example of the 2-D 1σ and 2σ marginalised results of one of the MC z_{ph}-PDF fits compared to our full data set and median constraints. We find that they are consistent to within 2σ. On closer inspection of the z_{ph}-PDFs outputted from LEPHARE we found only a small fraction of objects in our final sample were poorly constrained and therefore their contribution to this fit would have minimal impact. Nevertheless, this remains an important quality check of our sample to the robustness of the final result. Furthermore, comparing our median results to those of W12 (right panel set of Figure 10) and Figure 11, we find our results are consistent to within their 1σ errors, although we constrain the parameters much more strongly due to the larger sample.

5.2 Main Sequence constraints - II

Table 5 shows our resulting power-law constraints as applied to the redshift bins in Figure 8. The term 'all-data' refers to our fits within each redshift slice to the full mass-complete galaxy distribution and the values in parenthesis are our re-calibrated MS fits. Firstly we note that the median and 'all-data' fits are fully consistent within

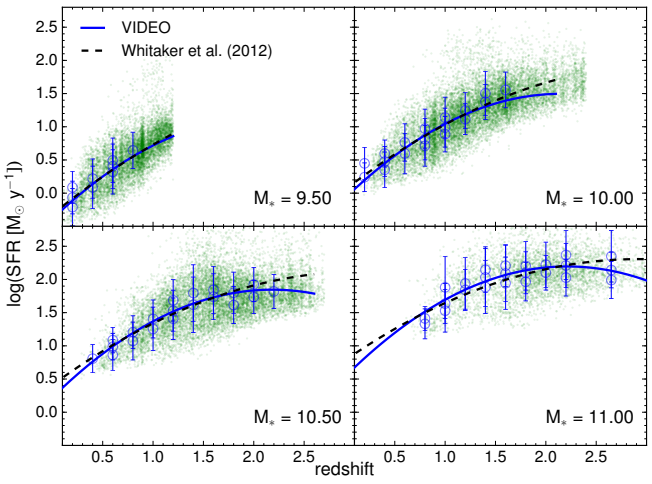

Figure 11. SFR versus redshift for the SFGs in our sample, in stellar mass bins of $\log_{10}(M_*/M_\odot)$ = 9.5, 10.0, 10.5 and 11.0. In each panel the green points show the galaxy distribution, and the blue circles denote the median values used in the fit from Figure 8. The redshift-dependent fit to the median points (Equation 6) is shown as the blue solid line. The black dashed line is the best fit from Whitaker et al. (2012) shown for comparison.

1σ and, as also found in the previous section, we observe strong evolution in the normalisation (β) consistent with the picture of an overall increase in star formation rate, at a given stellar mass, with redshift. In particular we observe a steady decline in SFR for a fixed stellar mass of $\log_{10}(M_*/M_\odot)\sim$10.0 by a factor of $\sim$ 19 from $z \sim 2$ to $z \sim 0.2$. In the following sections we compare our results to the broader literature that coincide at three selected redshift ranges $0.1 < z < 0.8$, $0.8 < z < 1.2$ and $1.9 < z < 2.1$. We use the calibrated MS fits as discussed in § 4.1 which are shown in Table 4 and Figure 12. In all three panels our results are shown as the blue line with the error on the fits shown as a shaded blue region.

5.2.1 *Comparison at $z \sim 0.45$*

In Figure 12 we show our fits to the 'all-data' case (denoted by the blue shaded region). In the left-hand panel of the figure our data covers a redshift range of $0.10 < z \leq 0.80$ with a stellar mass complete sample of 7487 galaxies. At this redshift we find $[\alpha, \beta] = [0.70 \pm 0.01, -6.46 \pm 0.06]$, which are fully consistent with Noeske et al. (2007a) who found $[0.67 \pm 0.08, -6.00 \pm 0.78]$ (black solid line), Santini et al. (2009) $[0.70 \pm 0.14, -6.27 \pm 1.54]$ (dashed black line) and Oliver et al. (2010) $[0.73 \pm 0.05, -6.86 \pm 0.55]$ (red squares). The radio stacking results by Dunne et al. (2009) find a much steeper gradient to ours with constraints $[\alpha, \beta] = [0.83 \pm 0.01, -7.83 \pm 0.13]$. In the case of Whitaker et al. (2012), their data was fitted using the redshift-dependant polynomial model of Equation 6, which is represented by the yellow solid line. Since their redshift binning is not aligned with ours we cannot make a straightforward power-law fit comparison, however, as we can see in the left panel of Figure 12, their fit seems very closely aligned with that of Noeske et al. (2007a) in both normalisation and slope over this redshift range. In Figure 13 we show the power-law fit to their data for each redshift bin (shown as black solid circles) and we find good agreement with our result over this redshift range.

Table 4. Power-law contraints from Figure 12. The numbers in parenthesis are those calibrated by Speagle et al. (2014) and which were used in the plotting of the Figure. Details of our calibration can be found in § 4.1.

Redshift	α	β
$0.1 < z < 0.8$		
This work	0.70 ± 0.01	-6.36 (-6.46) $\pm$ 0.06
Dunne et al. (2009)	0.83 ± 0.01	-7.92 (-7.83) $\pm$ 0.13
Noeske et al. (2007b)	0.67 ± 0.08	-6.19 (-6.00) $\pm$ 0.78
Oliver et al. (2010)	0.73 ± 0.05	-7.02 (-6.86) $\pm$ 0.55
Santini et al. (2009)	0.70 ± 0.14	-6.33 (-6.27) $\pm$ 1.54
$0.8 < z < 1.2$		
This work	0.70 ± 0.01	-5.92 (-6.02) $\pm$ 0.07
Dunne et al. (2009)	0.83 ± 0.05	-7.38 (-7.39) $\pm$ 0.53
Elbaz et al. (2007)	0.90	-8.14 (-8.06)
$1.9 < z < 2.1$		
This work	0.84 ± 0.04	-7.01 (-7.13) $\pm$ 0.28
Daddi et al. (2007)	0.90	-7.60 (-7.52)
Dunne et al. (2009)	0.88 ± 0.03	-7.21(-7.36) $\pm$ 0.37
Pannella et al. (2009)	0.95 ± 0.07	-8.30 (-8.35)
Reddy et al. (2012)	0.97 ± 0.05	-8.28 (-8.32) $\pm$ 1.28
Rodighiero et al. (2011)	0.79	-6.42 (-6.36)
Santini et al. (2009)	0.85 ± 0.17	-7.24 (-7.15) $\pm$ 1.87
Zahid et al. (2012)	0.46 ± 0.07	-2.99 (-2.94) $\pm$ 0.70

In a similar way, Magnelli et al. (2014) modelled their data with a quadratic given by Equation 4. In this case we have averaged their results over their two redshift ranges $0.20 < z \leq 0.50$ and $0.50 < z \leq 0.80$ to obtain an approximate comparison. Whilst their data supports a turnover toward the higher stellar masses, there appears to be a good agreement up to $\log_{10}(M_*/M_\odot)\sim$10.5 at which point their fit diverges. Although we note that no errors on their parameter constraints were reported in their analysis. Schreiber et al. (2015) also model their data in such a way as to allow for a SFR turnover (Equation 5) which we can observe at this redshift similar to that of Magnelli et al. (2014).

As with Whitaker et al. (2012), the binning of Rodighiero et al. (2010) are also not aligned with ours. However, we show our fits to their data in Figure 13, and for illustrative purposes have interpolated their fits to show their results in Figure 12. As a cross-check we fitted their data to the redshift-dependent model Equation 6 and found these fits to be consistent with our interpolated results. At this redshift their results show a slightly shallower slope of $\alpha = 0.60$ and normalisation $\alpha = -5.38$.

It is perhaps not too surprising that there is, in general, very good agreement between the results shown here at this relatively low redshift, since there is less likely to be residual contamination from passive galaxies which could result in shallower slopes.

5.2.2 *Comparison at $z \sim 1$*

As we move to the intermediate redshift bin $0.80 < z \leq 1.2$ shown in the middle panel of Figure 12, we have a total of 7746 galaxies in our stellar mass complete sample. Here we find very little difference from our result at $z \sim 0.45$ where $[\alpha, \beta] = [0.70 \pm 0.01, -6.02 \pm 0.07]$. However, we now begin to see more divergent trend between data-sets. For example, Elbaz et al. (2007) (black solid line) found a slope $\alpha = 0.9$, close to unity and a significantly lower normalisation of $\beta = -8.14$. A similar trend was found by Dunne et al. (2009) with $[\alpha, \beta] = [0.83 \pm 0.05, -7.39 \pm 0.53]$

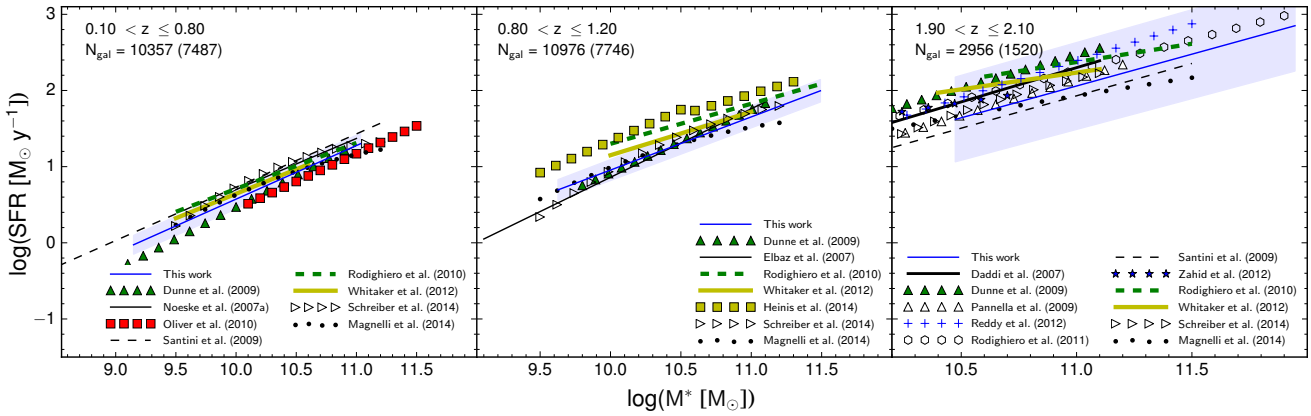

Figure 12. Comparison of the SF-MS. Our fits to the data are shown by the thin blue line with the error shown as the light blue shaded region. For each panel we find a slope $\alpha = 0.70 \pm 0.01$, 0.70 ± 0.01 and 0.83 ± 0.02 at $z \sim 0.45$, 1 and 2 respectively. Where possible we have shown comparative measurements within their respective stellar mass ranges from Noeske et al. (2007b); Daddi et al. (2007); Elbaz et al. (2007); Santini et al. (2009); Dunne et al. (2009); Pannella et al. (2009); Rodighiero et al. (2010); Oliver et al. (2010); Elbaz et al. (2011); Rodighiero et al. (2011); Zahid et al. (2012); Reddy et al. (2012); Whitaker et al. (2012); Heinis et al. (2014); Magnelli et al. (2014) and Schreiber et al. (2015). It should be noted that the symbols are not data points but merely indicate the power-law fit. The fits by Heinis et al. (2014) in the middle panel were estimated at $z \sim 1.4$ using a broken power-law (see text for details).

Table 5. Parameter constraints for $\log_{10}(\mathrm{SFR}) = \alpha \log_{10}(M_*) + \beta$. The redshift slices correspond to those in Figure 8. Columns 2 and 3 the fits to the median values of SFR. Columns 4 and 5 are fitted to the full distribution of data points. The values in parenthesis are our re-calibrated fits from M05 to BC03 SPS models (see § 4.1 for details).

	median fit		all data fit	
Redshift slice	β	α	β	α
$0.10 < z \leq 0.30$	$-7.86\ (-7.98) \pm 2.30$	0.82 ± 0.24	$-7.64\ (-7.76) \pm 0.20$	0.80 ± 0.02
$0.30 < z \leq 0.50$	$-6.27\ (-6.37) \pm 2.18$	0.68 ± 0.22	$-6.35\ (-6.45) \pm 0.13$	0.69 ± 0.01
$0.50 < z \leq 0.70$	$-5.65\ (-5.74) \pm 2.35$	0.63 ± 0.23	$-5.73\ (-5.82) \pm 0.13$	0.64 ± 0.01
$0.70 < z \leq 0.90$	$-4.79\ (-4.88) \pm 2.05$	0.56 ± 0.20	$-5.60\ (-5.69) \pm 0.11$	0.65 ± 0.01
$0.90 < z \leq 1.10$	$-6.10\ (-6.21) \pm 2.23$	0.71 ± 0.21	$-5.69\ (-5.79) \pm 0.11$	0.68 ± 0.01
$1.10 < z \leq 1.30$	$-5.75\ (-5.86) \pm 2.59$	0.69 ± 0.25	$-5.86\ (-5.96) \pm 0.12$	0.71 ± 0.01
$1.30 < z \leq 1.50$	$-4.94\ (-5.03) \pm 3.49$	0.63 ± 0.33	$-5.07\ (-5.16) \pm 0.17$	0.64 ± 0.02
$1.50 < z \leq 1.70$	$-4.94\ (-5.03) \pm 3.79$	0.64 ± 0.35	$-5.35\ (-5.45) \pm 0.18$	0.68 ± 0.02
$1.70 < z \leq 1.90$	$-5.47\ (-5.57) \pm 4.26$	0.69 ± 0.39	$-5.93\ (-6.04) \pm 0.23$	0.73 ± 0.02
$1.90 < z \leq 2.10$	$-5.93\ (-6.04) \pm 4.53$	0.73 ± 0.41	$-7.00\ (-7.12) \pm 0.28$	0.83 ± 0.03
$2.10 < z \leq 2.30$	$-7.36\ (-7.49) \pm 5.30$	0.87 ± 0.48	$-7.86\ (-8.00) \pm 0.40$	0.92 ± 0.04
$2.30 < z \leq 3.00$	$-7.44\ (-7.58) \pm 4.94$	0.88 ± 0.44	$-6.54\ (-6.66) \pm 0.33$	0.80 ± 0.03

(green triangles). In contrast, Rodighiero et al. (2010) find a shallowing slope of α to 0.52. At this redshift our results are more aligned with Whitaker et al. (2012) and Magnelli et al. (2014). We also note that Santini et al. (2009) found a slope that becomes shallower between $0.6 < z < 1.5$ from $\alpha = 0.73$ at $z \sim 0.8$ to $\alpha = 0.65$ at $z \sim 1.2$. With our D4000 SFG selection criteria we do not find strong evidence for a turnover in the SF-MS relation, however, we find that over this redshift range our results are consistent with those of Magnelli et al. (2014) (black dotted line) and Schreiber et al. (2015) (right triangles), at least up to $M_* \sim 10.5$. The results shown by Heinis et al. (2014) are consistent with ours with a modelled power-law giving $[-5.7 \pm 0.7, 0.70 \pm 0.07]$. However, they found a broken power-law a better fit to their data at this redshift finding a slope of ~ 0.85 for $M_* < 10^{10.5} M_\odot$ and a turning over to ~ 0.5 at the high mass end (shown as yellow squares in the Figure). In Section 5.4 we will explore the sensitivity of our modelling with respect to how SFGs are selected.

5.2.3 *Comparison at* $z \sim 2$

Finally, in the third panel we show the SF-MS over the redshift range $1.90 < z \leq 2.10$, with 1683 galaxies considered in the fit. Here we find significant positive evolution of the slope towards unity with $[\alpha, \beta] = [0.84 \pm 0.04, -7.13 \pm 0.28]$. Here we find separations in the magnitude of the slopes. In general Rodighiero et al. (2010), Whitaker et al. (2012), Zahid et al. (2012) and Magnelli et al. (2014) favour a much shallower slope of $\alpha \sim 0.45$, whereas we, along with Daddi et al. (2007); Dunne et al. (2009); Santini et al. (2009); Rodighiero et al. (2011); Pannella et al. (2009) and Reddy et al. (2012), find the opposite, with a range $0.79 \lesssim \alpha \lesssim 0.97$. Schreiber et al. (2015) also reported a steeper relation towards higher redshifts with a turnover only observed in the lower redshift regime. It should be noted that the uncertainties on the parameters for the power-law fits within each redshift bin for the Whitaker et al. (2012) data are large, of the order $\sigma_\alpha \sim 0.75$, which means that their results are formally consistent with ours at this redshift. The differences in α are perhaps better seen in Figure 13, which

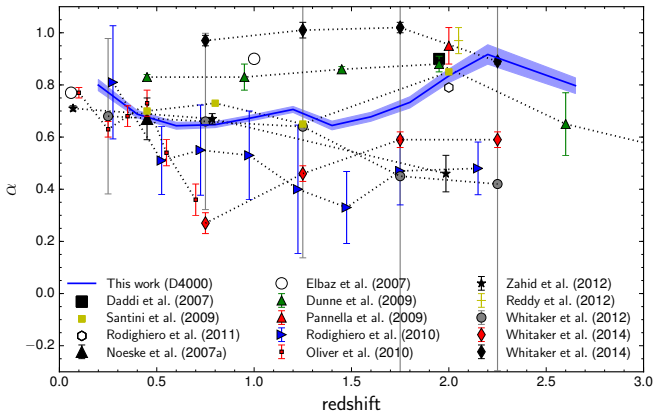

Figure 13. Comparison of the power-law slope α constraints as a function of redshift. The blue line and shaded error region is our fiducial result when we apply our $D4000$ selection. The legend indicates comparative works from Noeske et al. (2007b); Daddi et al. (2007); Elbaz et al. (2007); Santini et al. (2009); Dunne et al. (2009); Pannella et al. (2009); Rodighiero et al. (2010); Oliver et al. (2010); Elbaz et al. (2011); Rodighiero et al. (2011); Zahid et al. (2012); Reddy et al. (2012), Whitaker et al. (2012) and Whitaker et al. (2014) as also compared in Figure 12. The Whitaker et al. (2014) data represent fits for log stellar masses < 10.2 (solid red diamonds) and > 10.2 (solid black diamonds).

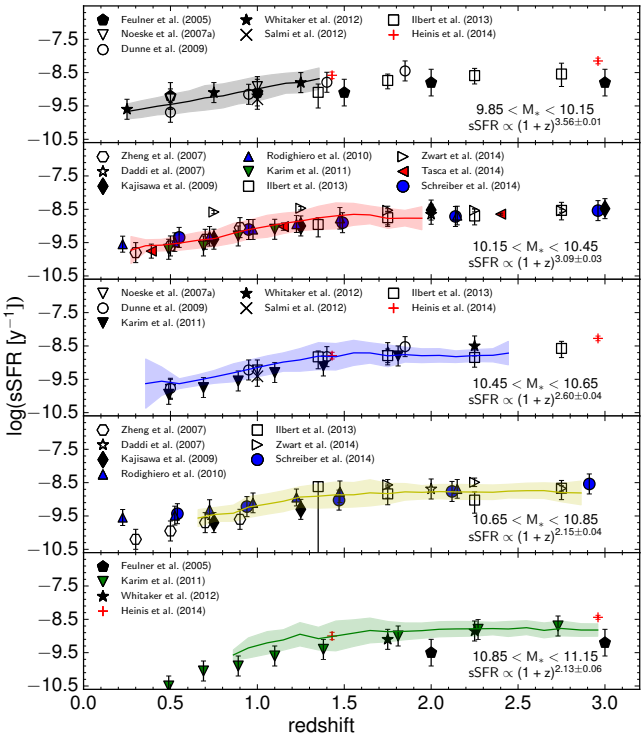

Figure 14. SSFR evolution. On each panel we show our median values of SSFR as a function of redshift for a range of log stellar masses centred on $\log_{10}(M_*/M_\odot)$=10.0,10.3,10.55,10.75 and 11.0, shown as black, red, blue, yellow and green shaded regions respectively. The statistical uncertainty is the combined error on the median and the cosmic variance i.e. $\sigma_{\rm tot}$=$\sqrt{(\sigma^2_{\rm MAD} + \sigma^2_{\rm V})}$. The other sSFR measurements are from Feulner et al. (2005); Noeske et al. (2007b); Daddi et al. (2007); Dunne et al. (2009); Kajisawa et al. (2009); Rodighiero et al. (2010); Karim et al. (2011); Salmi et al. (2012); Whitaker et al. (2012); Ilbert et al. (2013); Zwart et al. (2014); Tasca et al. (2014), and Schreiber et al. (2015).

Table 6. Parameter constraints for (sSFR / yr^{-1}) = $A + \gamma \log_{10}(1+z)$ for a range of fixed stellar masses as shown in Figure 14.

Stellar mass range $\log_{10}(M_*/M_\odot)$	Redshift range	A	γ
$9.85 < M_* < 10.15$	$0.25 < z \leq 1.35$	-10.05 ± 0.01	3.56 ± 0.01
$10.15 < M_* < 10.45$	$0.27 < z \leq 1.95$	-10.05 ± 0.01	3.09 ± 0.03
$10.45 < M_* < 10.65$	$0.36 < z \leq 2.44$	-10.03 ± 0.01	2.60 ± 0.04
$10.65 < M_* < 10.85$	$0.65 < z \leq 2.86$	-9.88 ± 0.01	2.15 ± 0.04
$10.85 < M_* < 11.15$	$0.86 < z \leq 2.96$	-9.94 ± 0.01	2.13 ± 0.06

shows that the magnitude of α in our sample clearly begins to rise at $z \gtrsim 1.5$ and e.g. Whitaker et al. (2012) begins to fall.

5.3 Evolution of specific star-formation rate

An alternative way to probe star formation histories over cosmic time is to look instead at the specific star formation rate (sSFR). This is simply given by sSFR=SFR/M_* which allows us to probe star formation per unit stellar mass. In Figure 14 we show how the sSFR evolves as a function of redshift for our sample of SFGs for stellar-mass bins, centred on $\log_{10}(M_*/M_\odot)$= 10.0, 10.3, 10.5, 10.75 and 11.0. The redshift ranges we probe within each mass bin are consistent with our mass completeness limits. We again compare our findings with other available sSFR measurements from the literature, as indicated in Figure 14. Our results are entirely consistent with other work out to $z \sim 3$ within our stellar-mass completeness limits, with our data showing a flattening off in the evolution of the sSFR beyond $z > 1.5$ for our highest stellar-mass bins.

We parameterise the redshift evolution of the sSFR for each stellar mass bin with (sSFR / yr^{-1}) = $A + \gamma \log_{10}(1+z)$. These results are shown in Table 6. We find that between mass bins 10.3 and 10.5 the relation evolves from $\gamma = 3.09$ to 2.60 out to a redshift of 1.95 and 2.44, respectively. This result is consistent with that of the recent work from Tasca et al. (2014) who found $\gamma = 2.8 \pm 0.2$ over a similar redshift range for fixed stellar mass of $\log_{10}(M_*/M_\odot) \sim 10.3$ using VUDS. Overall, we find a general flattening of the relation with redshift as we move to our highest stellar mass bin of $\log_{10}(M_*/M_\odot)$=11 with $\gamma = 2.13 \pm 0.06$ and normalisation of $A = -9.94 \pm 0.01$ between $0.85 < z < 2.96$.

If we restrict the redshift range out to $z < 1.4$, following Ilbert et al. (2014), we find a similar, but slightly steeper evolution with γ=[3.39±0.01, 3.57±0.04, 3.39±0.05, 3.58±0.22, 3.91±0.36] for respective mass bins of $\log_{10}(M_*/M_\odot)$= 9.5-10.0, 10-10.5, 10.5-11 and 11-11.5. In their work they found a similar mass-dependent evolution in sSFR with γ=[2.88±0.12, 3.31±0.10, 3.52±0.15, 3.78±0.60]. Why we find steeper slope at $\log_{10}(M_*/M_\odot)$= 10 remains unclear. However, we do note that at this mass range our fit was limited to $z \lesssim 1.35$ due to our completeness limits. If we relax our SFG D4000 selection cut from e.g. 1.3 to 1.35, which would introduce an older population of galaxies into our sample, we find that this has only marginal affect. Alternatively, if we instead use a *u-r* colour selection as discussed in § 3.3, this only really affects the high mass bins which is consistent with our findings in § 5.4. Of course there remains the possibility of numerous options within CIGALE that could be explored in more detail, but we reserve this for future work.

Nevertheless, within the redshift range we are considering in this work, we find very good agreement across a broad range of related works, that shows an in increasing mass-dependent evolution

with stellar mass below $z \sim 2$, which then begins to slow considerably beyond this redshift.

5.4 Star-forming selection effects and the high-mass turn over

As we discussed in § 4.1, the majority of off-sets added to calibrate the MS relation changes only the normalisation. However, the slope of the SF-MS is sensitive to effects such as how SFGs are selected (e.g. Oliver et al. 2010; Whitaker et al. 2012; Rodighiero et al. 2014; Speagle et al. 2014; Sobral et al. 2014; Ilbert et al. 2014). As shown in Figure 13 there is a broad range in the constrained values of α as a function of redshift across the literature. In the left panel of Figure 15 we compare our D4000 cut (red region) with the rest-frame *u-r* colour selection (blue region) and we can see that between $0.4 \lesssim z \lesssim 1$ there is a distinct shallowing of α applying our colour cut, which is a result of the flattening of the SF-MS at stellar masses $\gtrsim 10.5\ M_{\odot}$.

This is shown more clearly in Figure 16 where we show the SFR versus M_* relation, over the redshift slice $0.8 < z \leq 1.2$. The left-hand panel shows the full SFR-M_* distribution prior to any selection for SF galaxies. In the middle panel we show the resulting distribution once we impose the *u-r* colour cut, and finally the right panel shows our D4000 cut. It is clear that with a *u-r* colour cut there remains a residual population that, with the D4000 selection, would be considered a more passive population. This results in the median points having lower SFRs toward the high mass end. Thus, the resulting fit is shallower than that of the D4000 cut. Using the *u-r* we thus find similar model constraints to those of Magnelli et al. (2014) and Whitaker et al. (2014) applying the quadratic model of Equation 4. This fit is shown as the blue line where we find $[A1, A2, A3] = [-24.596, 4.626, -0.206]$. Over the same redshift range Magnelli et al. (2014) found [-26.51, 4.77, -0.202] and in Whitaker et al. (2014) they found $[-27.4 \pm 1.9, 5.0 \pm 0.4, -0.22 \pm 0.02]$ at $0.5 < z < 1.0$ and $[-26.0 \pm 1.7, 4.6 \pm 0.3, -0.19 \pm 0.02]$ at $1.0 < z < 1.5$. Although our results using a *u-r* colour selection show consistency in the model parameter fits to previous work, this is more likely due to residual contamination by an older sub-population of galaxies due to applying the *u-r* cut.

In addition, if we apply a more relaxed cut in D4000 from 1.3 to 1.35, thus allowing a slightly older galaxy population into our sample we can also observe the turnover in our median trends. This is demonstrated in the right hand panel of Figure 15, where the black stars are our fiducial result of D4000$<$1.3 and the red squares are from Whitaker et al. (2014). As we can see, with the cut at D4000 $<$1.3, our results are consistent with a constant slope out to high mass. However, with a cut at D4000 $<$1.35, the slope flattens at $\log_{10}(M_*/M_{\odot}) \gtrsim 10.5$. These tests highlight our sensitivity of our fits to the initial selection of SFGs.

Lastly, if we look at Table 2 the majority of works we compare to (including our own) have selected samples over an area of $\lesssim 1$ deg^2. At these scales uncertainties due to cosmic variance can become important particularly at the high mass end. In our work and that of e.g. Ilbert et al. (2013) this has been included in the model constraints, however, it is unclear as to whether other works consider this effect in their analysis.

6 COMPARISON WITH SIMULATIONS

In this section we compare our results for the SF-MS with a variety of simulations, performed with a number of different methods, to help elucidate the key physical processes that dictate the evolution of massive galaxies.

6.1 Hydrodynamical simulations

From the hydrodynamical approach we look at the Horizon (Dubois et al. 2014), Illustris (Sparre et al. 2014) and the Davé et al. (2013) (D13) simulations. As well as hydrodynamics and gravity, this genre of simulations typically include varying prescriptions of star formation, gas cooling and heating, and feedback from stellar winds, supernovae and AGN. Discussion on the relative merits of the various simulations is beyond the scope of this paper, however, we do note that they each probe varying volumes and resolutions: Illustris use a box size of 106.5 Mpc h^{-1} on the side with 1820^3 DM particles and 1820^3 gas cells with particle and gas target masses of $6.26 \times 10^6\ M_{\odot}$ respectivley. Horizon have similar volume of 100 Mpc h^{-1} on the side with 1024^3 dark matter (DM) particles of mass $8 \times 10^7\ M_{\odot}$, and D13 used the GADGET-2 N-body + Smoothed Particle Hydrodynamics Springel et al. (2005) to evolve their simulations, within a volume of 32 Mpc h^{-1} on the side containing 512^3 gas particles of mass $4.5 \times 10^6\ M_{\odot}$.

6.2 Scaling relation approaches

Behroozi et al. (2013) parameterised the stellar mass–halo mass (M_*-M_h; SMHM) scaling relation to model observed star-formation histories out to $z = 8$. By applying a MCMC approach to constrain their 15 free parameters, they begin with an initial guess for the SMHM relation, then find galaxy growth histories by applying the SMHM relation to dark matter merger trees. They then derive a series of inferred stellar mass functions and SFRs onto which they apply simulated observational errors and biases. Finally they compare their model to available data to constrain the SMHM relation.

The recent work by Mitra et al. (2014) (M14) is an analytical based approach which also exploits the use of observed scaling relations. In their approach they begin with a mass balance equation to model the inflows and outflows in the interstellar medium (ISM) assuming galaxies grow along a slowly-evolving equilibrium between accretion, feedback and star formation (e.g. Finlator & Davé 2008). In essence, the parameters of the equilibrium model describe the motion of gas into and out of galaxies, which is termed the *baryon cycle*. In their modelling they have only 8 free parameters that are constrained via a MCMC, comparing their model to the M_*-M_h constraints of Behroozi et al. (2013) and Moster et al. (2013), as well as the M_*-metallicity scaling relation from e.g. Andrews & Martini (2013); Zahid et al. (2014) and Steidel et al. (2014), out to $z \sim 2$.

Thus, by design, these types of approaches should be able to better reproduce the observed SFR-M_* relations compared to hydrodynamical and SAM simulations.

6.3 Results

In Figure 17 we show the SF-MS at $z = 1$ (left) and 2 (right). The blue solid line shows the fit to our data above our stellar mass completeness limit. The dotted blue line is an extrapolation of this fit for illustration purposes. The simulations show general agreement with the slope of the relation, but all have a lower normalisation in SFR by varying degrees. Perhaps as expected, the scaling relation approaches are most aligned with our work. By averaging over the

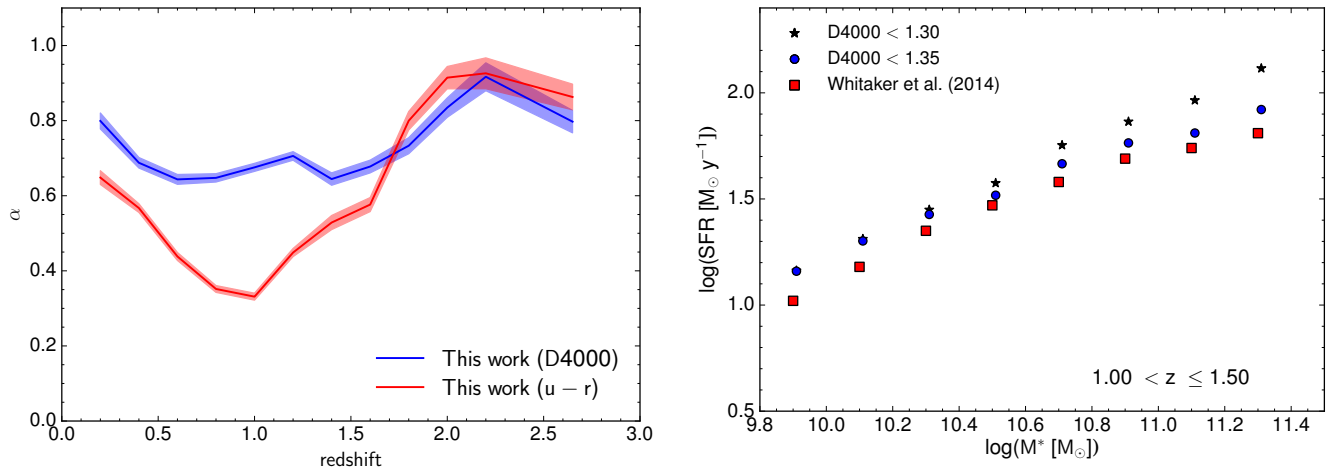

Figure 15. *Left:* Comparison of derived power-law slopes (α) as a function of redshift for our different SFG selection. The blue is for the D4000 ¡ 1.3 cut as was shown in Figure 13 and the red shows the results for a rest-frame *u-r* selection. *Right:* Comparing the high-mass turnover. The black stars show our fiducial result using an SFG criterion of D4000 $<$ 1.30. The blue circles show how our results change if we allow a slightly higher cut at 1.35, allowing older galaxies to be including in the SF-MS. We compare this to Whitaker et al. (2014) data shown as red squares which presented results with flattening of the SF-MS $\log_{10}(M_*/M_\odot) > 10.2$ dex.

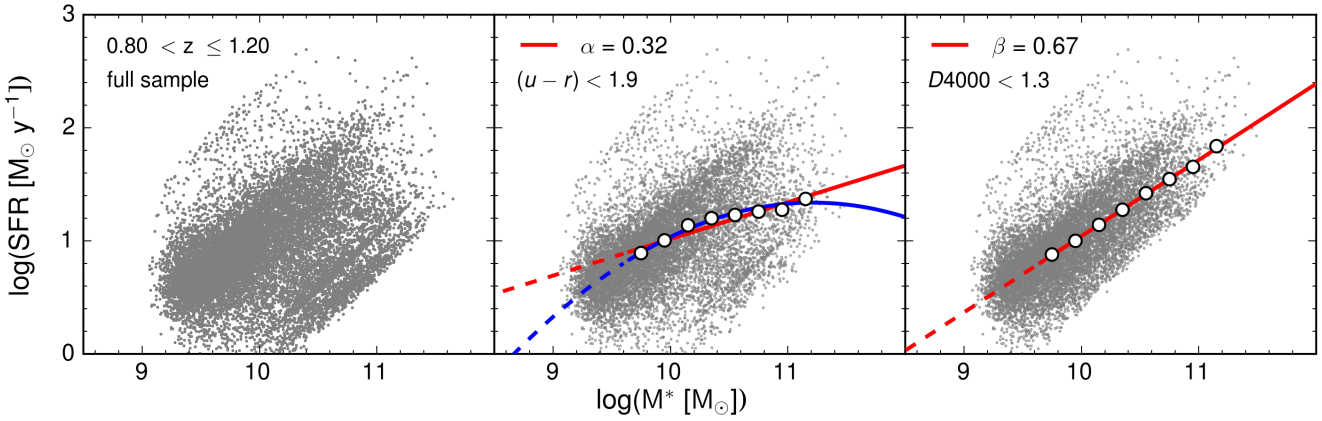

Figure 16. Comparison of the impact of different SFG selection methods on the SF-MS. The left panel shows the full sample at $z \sim 1$ that includes a passive population of galaxies. In the middle panel we show a star-forming sample applying a rest-frame *u-r* colour cut. The white solid circles are the median points of the distribution. The red solid line shows the resulting power-law fit for the stellar mass-complete sample yielding a slope of $\alpha = 0.29$; the dashed line is just the extrapolation of this fit below the completeness limit. The blue line shows a quadratic fit to the same median points which yielded coefficients of $A1$, $A2$, $A3$=[-21.527, 4.063, -0.1807] (see Equation 4). The right-hand panel now shows the star-forming sample if we use a D4000 index cut. The red line here shows a power-law slope of $\alpha = 0.66$.

stellar mass bins at 10, 10.5 and 11.0 we find M14 and B13 to be lower by a factor ~ 1.8. In contrast we find that the SF-MS from the hydrodynamics simulations of D13 and Illustris to be lower by as much as ~ 3 with Horizon showing the largest discrepancy being lower by a factor of $\sim$6. At $z = 2$ there is improvement in the normalisation of M14 and B13, with their models now being lower by factors of 1.4 and 1.2 respectively between M_* of 10.5 and 11. The hydrodynamics predictions show only a slight change from $z = 1$, and continue to significant under-predict the normalisation in the SF-MS relation.

It is worth noting that the Horizon simulation data set available to us, contains both SFGs and passive galaxies. Although we are unable to segregate them explicitly, we artificially impose a cut in SFR that closely mirrors our D4000 selection, shown in the bottom panels of Figure 17. As we can see there is only a marginal upward shift in the normalisation at $z = 1$ and very little change at $z = 2$, implying that the bulk of the simulated galaxies have significantly lower SFRs at a given stellar mass compared to the observations.

We now compare the observational results on the evolution of the sSFR (Figure 18), to the simulations, for the same range of stellar mass bins considered in § 5.3. If we consider redshifts $z < 1.0$ across all stellar mass bins, we find that M14, B13 and Illustris show good agreement with our results. At $1 < z < 2$ the Illustris predictions show an average factor of ~ 3 lower normalisation at $\log_{10}(M_*/M_\odot)$=10, which seems to reduce to 2 towards the highest stellar mass bin M_*= 11. We find both M14 and B13 continue to show very good agreement with our results across all stellar mass bins at $z > 1$. Finally, we again note that the Horizon simulations are lower by a factor of ~ 6 across all mass bins.

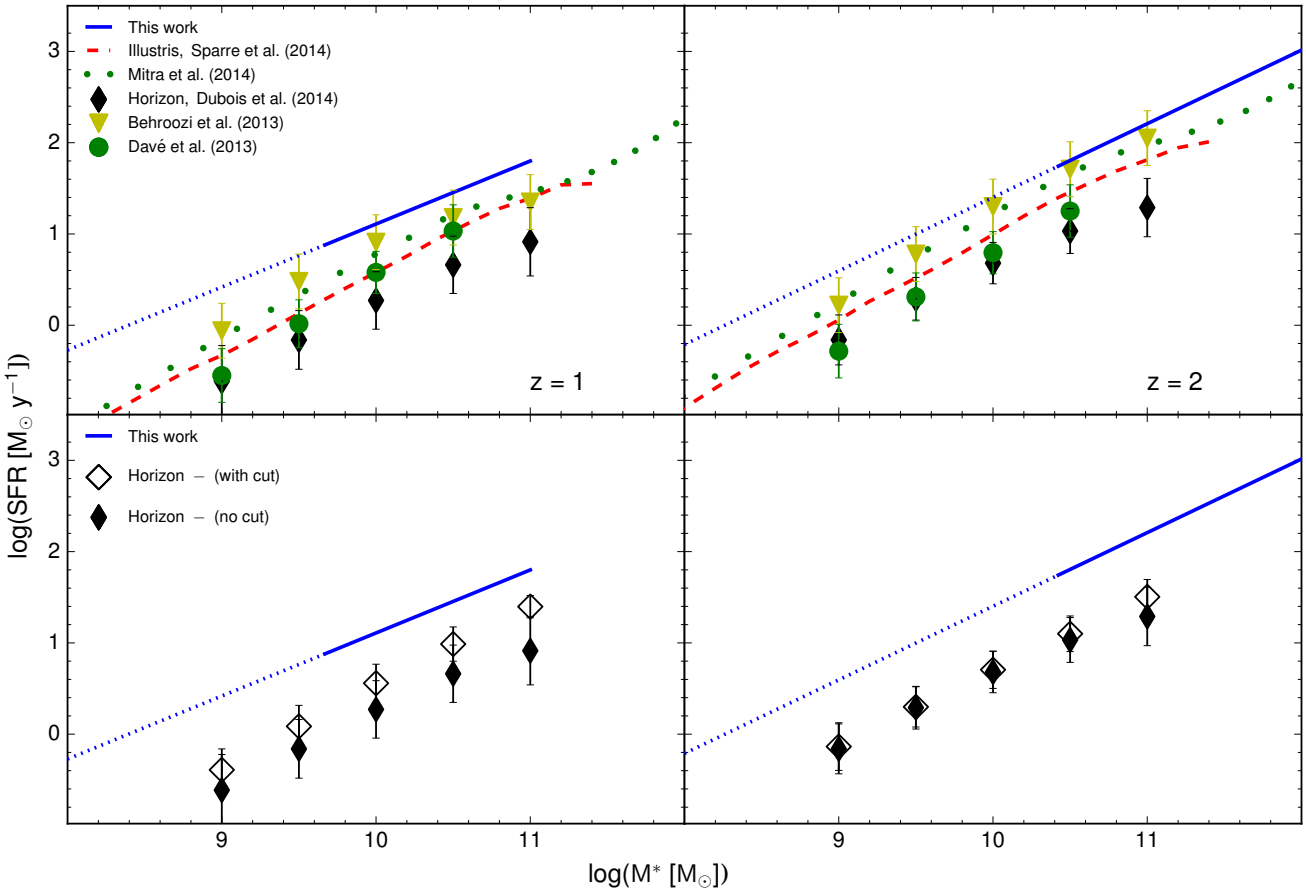

Figure 17. Comparison of the SFR-MS with current simulations. The shaded distribution of points with contours show our SFR-Mass results at $z \sim 1$ (left) and $z \sim 2$ (right). The fit to our data is shown as the solid blue line, with the dashed line extrapolated below our stellar mass completeness limit. The results from simulations at these redshifts are Illustris (Sparre et al. 2014, red solid line, hydro), Mitra et al. (2014) (green solid line, equilibrium model), Horizon (Dubois et al. 2014, black diamonds, hydro), Davé et al. (2013) (green dots, hydro) and Behroozi et al. (2013) (yellow triangles).

7 DISCUSSION

Theoretical predictions from the ΛCDM modelling of the average growth rate of dark matter halos through smooth cold accretion was well characterised to be $\propto (1+z)^{2.25}$ at $z \sim 2$ (Dekel et al. 2009). Developments in this area now favour a stronger evolution in sSFR to $\propto (1+z)^{2.5}$ (Dekel et al. 2013; Faucher-Giguère et al. 2011) which while lower than our constraints, is beginning to show convergence toward a higher evolution. In our comparison of the SFR-M_* and sSFR-z trends with the hydrodynamical simulations of Illustris (Sparre et al. 2014), Horizon (Dubois et al. 2014) and Davé et al. (2013) we found in all cases an under prediction of the normalisation by a factor ranging between ~ 2 (llustris and Davé et al. 2013) and 6 (Horizon). Such a disparity between observations and simulations, both in hydrodynamical and semi analytical modelling (SAMs), has been identified and discussed extensively (e.g. Daddi et al. 2007; Elbaz et al. 2007; Santini et al. 2009; Damen et al. 2009b; Davé et al. 2013; Sparre et al. 2014; Genel et al. 2014; Tasca et al. 2014). The general consensus shows at low redshifts ($z \lesssim 0.5$) simulations can reproduce the sSFR and again at $z \gtrsim 4$. However in the intermediate regime there remains a disconnect in the evolution of sSFR. Whilst there are a number of possible issues that may account for this effect that have been suggested such as: oversimplified gas accretion modelling, systematic offsets in gas cooling rates, insufficient sub-grid models that control star formation and stellar feedback, this remains an unresolved issue. Moreover, hydrodynamical and SAMs typically require ~ 20 and ~ 30-50 parameters respectively which can make drawing physical conclusions challenging.

Fundamentally, observations seem to be increasingly favouring the downsizing scenario, whereas simulated star formation histories are tied to the dark matter accretion histories and cannot produce the observed mass-dependence in sSFR (Damen et al. 2009b; Somerville & Davé 2014; Sparre et al. 2014).

The scaling relation based approaches of Behroozi et al. (2013) and Mitra et al. (2014) proved they could recover well the sSFR evolution across all mass ranges. This is perhaps not too surprising since their models are being constrained by current observational data. Nevertheless, they do present the opportunity to explore key physical aspects of galaxy formation within a relatively simple analytical framework compared to the full blown architecture of hydro and SAMs. In particular, the equilibrium model of Mitra et al. (2014) does not explicitly model halos, cooling, mergers or a disk star formation law, but instead parameterises the motion of gas into and out of galaxies, assuming that the gas reservoir in a galaxy is slowly evolving with an equilibrium between accretion, feedback, and star formation (Finlator & Davé 2008; Bouché et al. 2010). Their results suggest that mergers are sub-dominant

for overall galaxy growth and that the key drivers for the average evolution of SFGs is the continual smooth accretion regulated by continual outflows with occasional cycling.

Of course the way in which we select our SFGs plays a crucial role in the derived slopes of the SF-MS. In this work we demonstrated how two different SFG selection criteria can lead to very different constraints in the modelled SF-MS and, in particular, the high-mass turnover. From our comparisons to a wide range of related works there is a clear and well known bi-modal distribution in the slope of the SF-MS particularly beyond $z \sim 1$; where some find α around 0.5 and others close to unity. In Whitaker et al. (2014) using UV+IR derived SFRs they found a non evolving low mass ($\log_{10}(M_*/M_\odot)< 10.2$) MS slope close to unity. In contrast, they found an evolving and shallower high mass ($\log[M_*/M_\odot] >10.2$) slope that evolved to $\alpha = 0.59$ at $z \sim 2.25$. A similar turn-over has also recently been reported by Heinis et al. (2014); Magnelli et al. (2014); Schreiber et al. (2015). In Tasca et al. (2014) this has been interpreted as evidence of a more gradual star formation quenching progressing from high masses at high redshifts toward low masses at low redshifts. In the recent work by Buat et al. (2014) showed that the type of SFR indicator affects the normalisation of the MS and not the slope. However as discussed in e.g. Speagle et al. (2014); Ilbert et al. (2013) they way in which we select SFG can impact the slope considerably.

Our main approach was to select SFGs based on the D4000 index as outputted by CIGALE. This selection imposed a rather sharp cut in the SFR-M_* distributions which led to a roughly constant slope being derived out to $z \sim 1.7$ and little evidence for a high mass-turn over. However, when we instead applied a rest-frame *u-r* colour cut to isolate SFGs, we found strong evidence for a turn over at $\log_{10}(M_*/M_\odot)\sim 10.5$ which was consistent with the trends of the aforementioned works. However, we note that in both scenarios we found slopes of $\alpha \sim 0.8$ beyond $z \gtrsim 2$ that showed no sign of flattening at high mass which seems more inline with the trends of Schreiber et al. (2015).

The issue of which colour selection one should adopt to obtain a *clean* SF-MS has also been highlighted in e.g. Ilbert et al. (2013) and Speagle et al. (2014). Whilst using a mixture of different colour cuts to remove purely quiescent galaxies as in e.g. Ilbert et al. (2013) (*r-J,* NUV-*r*) does seem to provide a cleaner selection, the use of a D4000 cut within the SED fitting framework potentially gives us a more *physical* way of identifying an ageing population. This has been explored in recent work by Morokuma-Matsui et al. (2015) where they found the D4000 break as a cleaner way to select SFGs, albeit at low redshifts $z < 0.2$. Clearly this remains an ongoing issue that requires further investigation.

8 CONCLUSIONS

In this study we have used CFHTLS visible $ugriz$ and VIDEO near-infrared Z, Y, J, H, K_s photometry, along with the IRAC 3.6 and 4.5 μm bands from SERVS to investigate the evolution in the relation between stellar mass and star-formation rate to $z \sim 3$ using the public SED fitting code CIGALE to determine the SFR and stellar mass. Where available we included observations from SWIRE and HerMES for the longer wavelength data. CIGALE enforces an energetic balance between dust-enshrouded UV stellar emission and its re-emission in the IR, making the most of our multi-wavelength dataset.

We summarise our findings as follows:

- We propagated the full photometric redshift uncertainties in the form of their PDFs through CIGALE to provide more robust measurement of the SFR and stellar masses. In this work, the PDFs were estimated using LEPHARE and in general our results showed good consistency with an analysis which does not consider the PDFs, with no evidence for residual bias.
- By modelling the data with a simple power law we have found strong evolution in the normalisation of the SFR-M_* relation out to $z \sim 3$. For a fixed stellar mass of $\log_{10}(M_*/M_\odot)$=10.0 we find the median SFR decreases by a factor of ~ 19 from $z \sim 2$ to $z \sim 0.2$. This is consistent with the picture of quenching of star formation and downsizing.
- By selecting SFGs using a D4000 index cut we observe a nearly constant slope for the SF-MS out to $z \sim 1.7$ of $\alpha = 0.69\pm0.02$, beyond which we observe a rise, with $\alpha = 0.90\pm0.03$ at $z \sim 2.2$. At the highest redshift range probed, $2.3 < z < 3.0$ we find slightly lower values for the slope of $\alpha = 0.80 \pm 0.03$.
- However, when selecting on the basis of rest-frame *u-r* colour rather than the D4000 index, we found a slope that became progressively shallower out to $z \lesssim 1.7$, reaching a low value of $\beta \sim 0.35$ at $z \sim 1$. We found that in this scenario the SFR-M_* relation was more appropriately modelled by a broken power law or a quadratic, showing a turnover at $\log_{10}(M_*/M_\odot)\sim$10.5. This effect was also observed by relaxing our D4000 cut from 1.3 to 1.35 and thus allowing a slightly older population into our SF sample. On closer inspection we found that the *u-r* selection is not as efficient at removing the passive population and the turnover is largely due to a residual quiescent population that is not isolated. However, beyond $z \gtrsim 1.7$ our results are consistent with the trends of the D4000<1.3 selection, showing a steepening of $\alpha \sim 0.8$ out to $z \lesssim 3$.
- Our study of the sSFR with redshift from $z = 0.1$ to 3 found strong evolution. By modelling the data as sSFR $\propto (1+z)^\gamma$ we find a similar mass-dependent evolution out to $z \lesssim 1.4$ with $\gamma = 3.39\pm 0.01$ to $\gamma = 3.91 \pm 0.36$ from $\log_{10}(M_*/M_\odot)$=9.75 to 11.25 re-

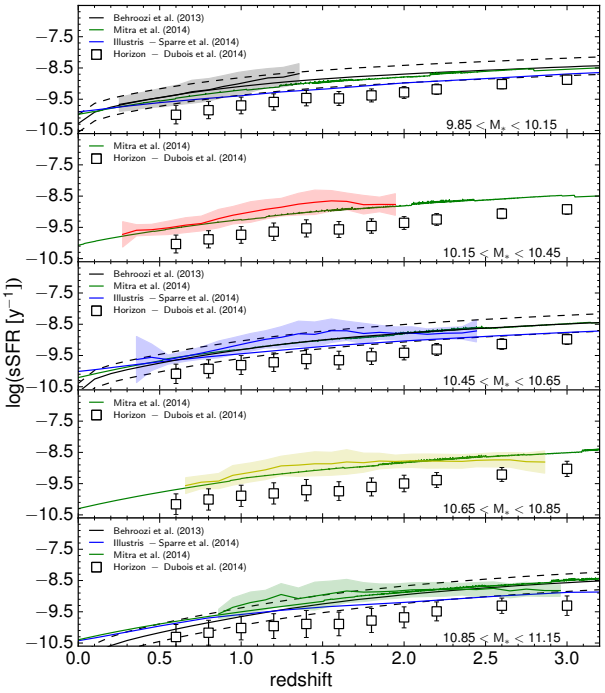

Figure 18. Same as Figure 14 but now comparing to simulations. Predictions are from Behroozi et al. (2013), Mitra et al. (2014), (Illustris, Genel et al. 2014; Sparre et al. 2014) and (Horizon, Dubois et al. 2014)

spectively. Extending this analysis to higher redshifts yielded $\gamma = 2.60 \pm 0.04$ for a stellar fixed mass of $\log_{10}(M_*/M_\odot)$=10.5 out to $z \sim 2.44$. At our highest stellar mass bin of $\log_{10}(M_*/M_\odot)$=11 we found a flattening in the relation with $\gamma = 2.13 \pm 0.06$ between $0.86 < z \lesssim 3$.

Finally, our current sample size has been limited to 1 deg^2 to allow comprehensive broadband coverage. However, the VIDEO survey will have a total coverage of 12 deg^2 on its completion, allowing us to probe a larger and deeper area and thus will provide some of the most concise measurements of the SFR-M_* relation, leading to greater insight into how this relates to the underlying dark matter distribution and its evolution with redshift.

ACKNOWLEDGMENTS

We would like to thank Veronique Buat, Denis Burgarella, Romeel Davé, Claudia Maraston, David Gilbank, Ros Skelton, Martin Hendry, Julien Devriendt, Duncan Farrah, Dan Smith, Daniel Cunnama and Jonny Zwart for useful discussions throughout this project. We are grateful to Giulia Rodighiero, Catherine Whitaker, Olivier Ilbert, Peter Behroozi, Sebastien Heinis, the Horizon and Illustris simulation teams, Sourav Mitra and Romeel Davé for providing their data products which proved to most helpful in our analysis. The bulk of observational sSFR data from Figure 14 were obtained from http://www.peterbehroozi.com/data.html

RJ, MV, MJ, MP, MS and EG acknowledge the support from the South African National Research Foundation and the Square Kilometre Array (South Africa). MV and MJ acknowledge support from the European Commission Research Executive Agency FP7-SPACE-2013-1 Scheme (Grant Agreement 607254)

Numerical computations were done on the Sciama High Performance Compute (HPC) cluster which is supported by the ICG, SEPNet and the University of Portsmouth.

Based on data products from observations made with ESO Telescopes at the La Silla or Paranal Observatories under ESO programme ID 179.A-2006 and was supported by the European Commission Research Executive Agency FP7-SPACE-2013-1 Scheme (Grant Agreement 607254 - Herschel Extragalactic Legacy Project - HELP).

REFERENCES

Andrews B. H., Martini P., 2013, ApJ, 765, 140
Balogh M. L., Morris S. L., Yee H. K. C., Carlberg R. G., Ellingson E., 1999, ApJ, 527, 54
Behroozi P. S., Wechsler R. H., Conroy C., 2013, ApJ, 770, 57
Bernstein J. P., et al., 2012, ApJ, 753, 152
Bouché N., et al., 2010, ApJ, 718, 1001
Bower R. G., Benson A. J., Malbon R., Helly J. C., Frenk C. S., Baugh C. M., Cole S., Lacey C. G., 2006, MNRAS, 370, 645
Bower R. G., McCarthy I. G., Benson A. J., 2008, MNRAS, 390, 1399
Bruzual G., Charlot S., 2003, MNRAS, 344, 1000
Buat V., et al., 2014, A&A, 561, A39
Burgarella D., Buat V., Iglesias-Páramo J., 2005, MNRAS, 360, 1413
Calzetti D., 1997, AJ, 113, 162
Calzetti D., Kinney A. L., Storchi-Bergmann T., 1994, ApJ, 429, 582
Calzetti D., Armus L., Bohlin R. C., Kinney A. L., Koornneef J., Storchi-Bergmann T., 2000, ApJ, 533, 682
Chabrier G., 2003, PASP, 115, 763
Charlot S., Fall S. M., 2000, ApJ, 539, 718
Chary R., Elbaz D., 2001, ApJ, 556, 562
Chen Y.-M., Wild V., Kauffmann G., Blaizot J., Davis M., Noeske K., Wang J.-M., Willmer C., 2009, MNRAS, 393, 406
Conroy C., 2013, ARA&A, 51, 393
Conroy C., Gunn J. E., White M., 2009, ApJ, 699, 486
Cowie L. L., Songaila A., Hu E. M., Cohen J. G., 1996, AJ, 112, 839
Daddi E., Cimatti A., Renzini A., Fontana A., Mignoli M., Pozzetti L., Tozzi P., Zamorani G., 2004, ApJ, 617, 746
Daddi E., et al., 2007, ApJ, 670, 156
Dale D. A., Helou G., 2002, ApJ, 576, 159
Damen M., Labbé I., Franx M., van Dokkum P. G., Taylor E. N., Gawiser E. J., 2009a, ApJ, 690, 937
Damen M., Förster Schreiber N. M., Franx M., Labbé I., Toft S., van Dokkum P. G., Wuyts S., 2009b, ApJ, 705, 617
Davé R., Oppenheimer B. D., Finlator K., 2011, MNRAS, 415, 11
Davé R., Katz N., Oppenheimer B. D., Kollmeier J. A., Weinberg D. H., 2013, MNRAS, 434, 2645
Dekel A., et al., 2009, Nature, 457, 451
Dekel A., Zolotov A., Tweed D., Cacciato M., Ceverino D., Primack J. R., 2013, MNRAS, 435, 999
Dubois Y., et al., 2014, MNRAS, 444, 1453
Dunne L., Ivison R. J., Maddox S., Cirasuolo M., Mortier A. M., Foucaud S., Ibar E., et al., 2009, MNRAS, 394, 3
Elbaz D., et al., 2007, A&A, 468, 33
Elbaz D., et al., 2011, A&A, 533, A119
Erb D. K., Steidel C. C., Shapley A. E., Pettini M., Reddy N. A., Adelberger K. L., 2006, ApJ, 647, 128
Faucher-Giguère C.-A., Kereš D., Ma C.-P., 2011, MNRAS, 417, 2982
Feulner G., Gabasch A., Salvato M., Drory N., Hopp U., Bender R., 2005, ApJ, 633, L9
Finlator K., Davé R., 2008, MNRAS, 385, 2181
Fioc M., Rocca-Volmerange B., 1997, A&A, 326, 950
Flaugher B., 2005, International Journal of Modern Physics A, 20, 3121
Fritz J., Franceschini A., Hatziminaoglou E., 2006, MNRAS, 366, 767
Genel S., et al., 2014, MNRAS, 445, 175
Giovannoli E., Buat V., Noll S., Burgarella D., Magnelli B., 2011, A&A, 525, A150+
Griffin M. J., et al., 2010, A&A, 518, L3+
Guo Q., White S. D. M., 2008, MNRAS, 384, 2
Hastings W. K., 1970, Biometrika, 57, 97
Heinis S., et al., 2014, MNRAS, 437, 1268
Hoaglin D. C., Mosteller F., Tukey J. W., 1983, Understanding robust and exploratory data anlysis
Hopkins A. M., Beacom J. F., 2006, ApJ, 651, 142
Ilbert O., et al., 2006, A&A, 457, 841
Ilbert O., et al., 2010, ApJ, 709, 644
Ilbert O., et al., 2013, A&A, 556, A55
Ilbert O., et al., 2014, preprint, (arXiv:1410.4875)
Jarvis M. J., et al., 2013, MNRAS, 428, 1281
Kajisawa M., et al., 2009, ApJ, 702, 1393
Karim A., Schinnerer E., Martínez-Sansigre A., Sargent M. T., van der Wel A., Rix H.-W., Ilbert O., et al., 2011, ApJ, 730, 61
Kashino D., et al., 2013, ApJ, 777, L8
Kauffmann G., et al., 2003, MNRAS, 341, 33
Kinney A. L., Calzetti D., Bohlin R. C., McQuade K., Storchi-Bergmann T., Schmitt H. R., 1996, ApJ, 467, 38
Kitzbichler M. G., White S. D. M., 2007, MNRAS, 376, 2
Kroupa P., 2001, MNRAS, 322, 231
Lee K.-S., et al., 2011, ApJ, 733, 99
Lee K.-S., et al., 2012, ApJ, 752, 66
Lewis A., Bridle S., 2002, Phys. Rev. D, 66, 103511
Lilly S. J., Le Fevre O., Hammer F., Crampton D., 1996, ApJ, 460, L1
Lonsdale C. J., et al., 2003, PASP, 115, 897
Madau P., 1995, ApJ, 441, 18
Magdis G. E., Rigopoulou D., Huang J.-S., Fazio G. G., 2010, MNRAS, 401, 1521
Magnelli B., et al., 2014, A&A, 561, A86
Maraston C., 2005, MNRAS, 362, 799
Mauduit J.-C., et al., 2012, PASP, 124, 714
Mitra S., Davé R., Finlator K., 2014, preprint, (arXiv:1411.1157)

Morokuma-Matsui K., Baba J., Sorai K., Kuno N., 2015, preprint, (arXiv:1501.02915)
Moster B. P., Somerville R. S., Newman J. A., Rix H.-W., 2011, ApJ, 731, 113
Moster B. P., Naab T., White S. D. M., 2013, MNRAS, 428, 3121
Muzzin A., et al., 2013, ApJS, 206, 8
Noeske K. G., et al., 2007a, ApJ, 660, L43
Noeske K. G., et al., 2007b, ApJ, 660, L47
Noll S., Mehlert D., Appenzeller I., Bender R., Böhm A., Gabasch A., et al., 2004, A&A, 418, 885
Noll S., Burgarella D., Giovannoli E., Buat V., Marcillac D., Muñoz-Mateos J. C., 2009, A&A, 507, 1793
Oliver S., et al., 2010, MNRAS, 405, 2279
Oliver S. J., et al., 2012, MNRAS, 424, 1614
Pannella M., et al., 2009, ApJ, 698, L116
Pforr J., Maraston C., Tonini C., 2012, MNRAS, 422, 3285
Pilbratt G. L., et al., 2010, A&A, 518, L1
Pozzetti L., et al., 2010, A&A, 523, A13
Prevot M. L., Lequeux J., Prevot L., Maurice E., Rocca-Volmerange B., 1984, A&A, 132, 389
Reddy N. A., Pettini M., Steidel C. C., Shapley A. E., Erb D. K., Law D. R., 2012, ApJ, 754, 25
Renzini A., Peng Y.-j., 2015, ApJ, 801, L29
Rodighiero G., et al., 2010, A&A, 518, L25
Rodighiero G., et al., 2011, ApJ, 739, L40
Rodighiero G., et al., 2014, MNRAS, 443, 19
Roseboom I. G., et al., 2010, MNRAS, 409, 48
Rowan-Robinson M., et al., 2008, MNRAS, 386, 697
Salimbeni S., et al., 2009, in Giobbi G., Tornambe A., Raimondo G., Limongi M., Antonelli L. A., Menci N., Brocato E., eds, American Institute of Physics Conference Series Vol. 1111, American Institute of Physics Conference Series. pp 207–211 (arXiv:0901.3540), doi:10.1063/1.3141545
Salmi F., Daddi E., Elbaz D., Sargent M. T., Dickinson M., Renzini A., Bethermin M., Le Borgne D., 2012, ApJ, 754, L14
Salpeter E. E., 1955, ApJ, 121, 161
Santini P., Fontana A., Grazian A., Salimbeni S., Fiore F., Fontanot F., et al., 2009, A&A, 504, 751
Schreiber C., et al., 2015, A&A, 575, A74
Shim H., Chary R.-R., Dickinson M., Lin L., Spinrad H., Stern D., Yan C.-H., 2011, ApJ, 738, 69
Smith D. J. B., et al., 2012, MNRAS, 427, 703
Sobral D., Best P. N., Smail I., Mobasher B., Stott J., Nisbet D., 2014, MNRAS, 437, 3516
Somerville R. S., Davé R., 2014, preprint, (arXiv:1412.2712)
Sparre M., et al., 2014, preprint, (arXiv:1409.0009)
Speagle J. S., Steinhardt C. L., Capak P. L., Silverman J. D., 2014, ApJS, 214, 15
Springel V., et al., 2005, Nature, 435, 629
Steidel C. C., et al., 2014, ApJ, 795, 165
Suzuki T. L., et al., 2015, preprint, (arXiv:1505.02410)
Tasca L. A. M., et al., 2014, preprint, (arXiv:1411.5687)
Vogelsberger M., et al., 2014, Nature, 509, 177
Walcher J., Groves B., Budavári T., Dale D., 2011, Ap&SS, 331, 1
Westra E., Geller M. J., Kurtz M. J., Fabricant D. G., Dell'Antonio I., 2010, ApJ, 708, 534
Whitaker K. E., et al., 2012, ApJ, 754, L29
Whitaker K. E., et al., 2014, ApJ, 795, 104
Zahid H. J., Dima G. I., Kewley L. J., Erb D. K., Davé R., 2012, ApJ, 757, 54
Zahid H. J., Dima G. I., Kudritzki R.-P., Kewley L. J., Geller M. J., Hwang H. S., Silverman J. D., Kashino D., 2014, ApJ, 791, 130
Zwart J. T. L., Jarvis M. J., Deane R. P., Bonfield D. G., Knowles K., Madhanpall N., Rahmani H., Smith D. J. B., 2014, MNRAS, 439, 1459
da Cunha E., Charlot S., Elbaz D., 2008, MNRAS, 388, 1595

This paper has been typeset from a TEX/LATEX file prepared by the author.